MONTE CARLO SIMULATION OF COSMIC RADIATION SHIELDING EFFICIENCY OF LOW DENSITY AND SMALL ATOMIC MASS NUMBER MATERIALS

DUMRONGSAK RODPHOTHONG

A THESIS SUBMITTED IN PARTIAL FULFILLMENT OF THE REQUIREMENTS FOR THE DEGREE OF DOCTOR OF PHILOSOPHY MAJOR IN PHYSICS FACULTY OF SCIENCE UBON RATCHATHANI UNIVERSITY YEAR 2018

ACKNOWLEDGEMENTS

I would like to thank my advisor, Asst. Prof. Dr. Tanin Nutaro for his instructions, valuable advisement and improvement, not only this thesis, but for the researches and project since I was in first year undergrad. I appreciate his patience, suggestions and supporting during the part year of developing this thesis.

Thanks go without saying to the thesis committee, Asst. Prof. Dr. Chanrungrit Channok and Asst. Prof. Dr. Nipon Gasiprong for their reading and criticizing the manuscript. Special thank go to Mr. Chalermpon Mutuwong and Mr. Chakrit Sri-wunkum for his assistance in typing a part of this thesis.

I would like to thank Dr. Alejandro Sáiz for his valuable advice, suggestions, support and techniques for using LINUX and FLUKA programming. Special thanks for my Mom, Dad and brother for their cheerfulness, love, care and all support they gave to me. Finally, I would like to thank the people who gave me suggestions, cheerfulness, support and companionship during the time I developed this thesis.

Dumrongsak Rodphothong
Researcher

บทคัดย่อ

เรื่อง : การจำลองเพื่อหาประสิทธิภาพการกำบังรังสีจากอวกาศด้วยวิธีแบบมอนติคาร์โล สำหรับวัสดุที่มีความหนาแน่นต่ำและเลขมวลน้อย

ผู้วิจัย : ดำรงศักดิ์ รอดโพธิ์ทอง

ชื่อปริญญา : ปรัชญาดุษฎีบัณฑิต

สาขาวิชา : ฟิสิกส์

อาจารย์ที่ปรึกษา : ผู้ช่วยศาสตราจารย์ ดร.ธานินทร์ นุตโร

คำสำคัญ : รังสีคอสมิก, การกำบังรังสี, โปรแกรมฟลุก้า

ได้จำลองเพื่อปรับปรุงการกำบังรังสีคอสมิกจากอวกาศด้วยโปรแกรมคอมพิวเตอร์ โดยมุ่งการประเมินประสิทธิภาพการกำบังรังสีไปที่วัสดุที่มีความหนาแน่นต่ำและมีค่าเลขมวลน้อย ทั้งนี้เมื่ออยู่ภายใต้แหล่งกำเนิดจากทั้งเหตุการณ์พายุสุริยะรุนแรง และอนุภาครังสีคอสมิกจากแกแลกซี จากนั้นจึงเทียบประสิทธิภาพกับวัสดุอลูมิเนียมซึ่งเป็นวัสดุหลักพื้นฐานในการสร้างยานอวกาศ การศึกษานี้ได้ใช้ไฮโดรเจนเหลว น้ำ และโพลีเอทาลีน เป็นวัสดุกำบังเพื่อเทียบผลที่ได้กับอะลูมิเนียม การประเมินค่าประสิทธิภาพการกำบังรังสีทำได้โดยการเปรียบเทียบข้อมูลโดสในวัสดุกำบังและในวัสดุที่ใช้เป็นเป้าซึ่งในที่นี้จะใช้น้ำ โดยใช้โปรแกรมการขนส่งแบบมอนติคาร์โลที่รู้จักดีคือฟลุกก้า การเทียบประสิทธิภาพสามารถทำได้โดยการกำหนดให้ค่าผลคูณของพื้นที่ผิวและความหนาแน่น มีค่าเท่ากันสำหรับวัสดุกำบังรังสีทุกตัว จากการศึกษาพบว่า ไฮโดรเจนเหลว โพลีเอทาลีนและน้ำ มีประสิทธิภาพในการกำบังรังสีได้ดีกว่าอะลูมิเนียมทั้งจากเหตุการณ์พายุสุริยะรุนแรง และรังสีคอสมิกจากแกแลกซี

ABSTRACT

TITLE : MONTE CARLO SIMULATION OF COSMIC RADIATION SHIELDING EFFICIENCY OF LOW DENSITY AND SMALL ATOMIC MASS NUMBER MATERIALS

AUTHOR : DUMRONGSAK RODPHOTHONG

DEGREE : DOCTOR OF PHILOSOPHY

MAJOR : PHYSICS

ADVISOR : ASST. PROF. TANIN NUTARO, Ph. D.

KEYWORDS : COSMIC RAYS, SHIELDING, FLUKA

We had performed computer simulations for improving the spacecraft shielding from cosmic radiation in space. It focuses on the evaluation of shielding efficiency of the low density with a small atomic mass number materials subjected to both SPEs and GCRs sources. Then we compared their effectiveness with aluminum which is the main primary metal used in spacecraft. In this study we used liquid hydrogen, water and polyethylene as shielding materials to compare with aluminum. The efficiency of a shield is evaluated by the dose profile within the shield and the amount of dose absorbed by water that we used as a target by using FLUKA which is a well known Monte Carlo transport code. The efficiency comparison is made by fixing the area density of a shielding material. It was found that liquid hydrogen, polyethylene and water outperform aluminum for both Solar Particle Events and Galactic Cosmic Ray.

CONTENTS

CONTENTS (CONTINUED)

LIST OF TABLES

LIST OF FIGURES

FIGURES **PAGE**

CHAPTER 1
INTRODUCTION

1.1 Overview

For space flights beyond the Earth's magnetosphere, both the crew and the spacecraft equipment faces a significant hazard from the natural ionizing radiation environment. The two sources of this radiation are Galactic Cosmic Rays (GCRs) and radiation from the Sun.

High energy GCR particles of all atomic numbers are showered into the galaxy when stars undergo supernova. Approximately 88% of all GCR particles are hydrogen, 10% are helium, and the remaining percentage consists of heavier ions. (Townsend, 2005) The flux of high-energy particles into the solar system is isotropic, arriving at any point in deep space with equal intensity from all directions, but is affected by the Sun's natural 11 year cycle. During periods of solar maximum, GCR intensity is reduced by the deflection of lower energy cosmic rays by the increased volume of plasma in the solar wind (See figure 1.1).

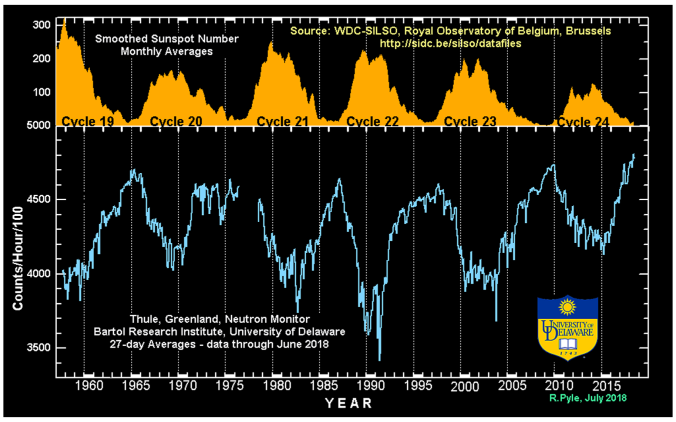

Figure 1.1 Solar modulation refers to influence the sun exerts upon the intensity of galactic cosmic rays. As solar activity rises(top panel), the count rate of galactic cosmic rays recorded by neutron monitor decreases(bottom panel).

Solar Cosmic Radiation is composed of two categories of radiation, low energy solar-wind particles that are constantly emitted from the sun (generally considered not to be dangerous), and highly energetic solar particle events (SPE). SPE-based radiation is a consequence of coronal mass ejections that originate from disturbed magnetic regions on the sun's surface. The typical 11 year cycle of the sun is characterized by a period of four years of relative inactivity, followed by seven years with increased numbers of SPE's. These ejections of high energy particles are highly directed, affecting only small regions of space, but are characterized by very high particle fluxes and can be extremely hazardous to space systems and crewed space vehicles.

Dosage from a radiative environment can be diminished via the use of radiation shielding. These shields consist of material that absorb or scatter incoming high-energy particles, protecting the personnel and equipment from ionizing radiation. In principle, these shields can be made of any material, but some exhibit better absorption and scattering properties than others.

The use of general-purpose particle interaction and transport Monte Carlo codes is often the most accurate and efficient choice for assessing radiation protection quantities. Due to the vast spread of such codes to all areas of particle physics and the associated extensive benchmarking with experimental data, the modeling has reached an unprecedented accuracy. Furthermore, most codes allow the user to simulate all aspects of a high energy particle cascade in one and the same run: from the first interaction of a TeV nucleus over the transport and re-interactions (hadronic and electromagnetic) of the produced secondaries, to detailed nuclear fragmentation.

1.2 Motivation

Since most space radiation are charged particles of high energy, they can cause damage to electronic equipment above Earth's atmosphere, such as in satellites, aircraft, etc., affecting communication and causing effects on the genetic structure of organisms. This provides motivation to support the study of space radiation and to try to protect expensive equipment and astronauts from the energetic space radiation.

The purpose of this study is to improve spacecraft shielding from radiation in space. It focuses on the evaluation of shielding efficiency of different materials. The efficiency of a shield is evaluated by the dose profile within the shield and the amount of dose absorbed by a target using the Monte Carlo transport code called FLUKA. The output of this code is validated by recreating the experiments from published papers and comparing the results. Once the FLUKA's output is validated, the efficiency of materials, subject to SPE and GCR sources, are evaluated.

This work will give us data for further analysis and better understanding of effects of cosmic radiation on humans and shielding from it. We will also obtain information that can be applied to improve space physics and astrophysics knowledge.

1.3 Objectives

1.3.1. Use FLUKA program in order to model various space radiation conditions, GCRs and SEPs source and simulate two models of the target (spherical and cylindrical).

1.3.2. Study shielding effectiveness of certain materials.It was found that the choice of material used for shielding has low density materials with small atomic mass numbers are usually the most efficient shields for both SPEs and GCRs.Therefore Liquid hydrogen,Water and polyethylene was chosen to simulate and compare their effectiveness with aluminum – the primary metal used in spacecraft.

1.4 Outline of the thesis

This thesis consists of five chapters. The first chapter overviews the work and the basic ideas of the research. The research motivations and objectives are mentioned here. Chapter 2, starting with the type of radiation in space.The basic concepts of radiation and the radiation effect on humans is described. In Chapter 3, We describe short summary of FLUKA, the program for calculations of particle transport and interactions with matter base on Monte Carlo simulations. For the radiation shielding simulations,we will explain the modeling of target and shielding structures and processes of the FLUKA program in Chapter 4. Finally, results discussion and the conclusions are included in the last chapter.

CHAPTER 2
LITERATURE REVIEW

This chapter examines relevant literature and the theoretical framework that informs the study of the space radiation.

2.1 Cosmic rays

Although the name would suggest that cosmic rays are some form of electromagnetic radiation, they are actually subatomic particles traveling at significant fractions of the speed of light. Primarily atomic nuclei (hydrogen and helium nuclei are the most common, but nuclei of all naturally occurring elements have been detected), whatever accelerates these nuclei to such high energies, does not appear to have the same effect on electrons which make up less than 1% of all cosmic rays.

Cosmic Ray energies span a truly enormous range, from about 10^7 eV through to 10^{20} eV, but at higher energies the numbers of cosmic rays drop off dramatically. Roughly speaking, for every 10% increase in energy, the number of cosmic rays per unit area falls by a factor of 1000. The cosmic ray spectrum measured at the top of the atmosphere are shown in Figure 2.1 (Swordy, 2001).

Since cosmic rays are charged particles whose paths are affected by magnetic fields, determining where they originate is a challenge, and for the most part, an unsolved mystery. For all but the highest-energy cosmic rays (which remain largely unaffected by the magnetic fields), astronomers cannot simply trace the path of the cosmic rays back to their origin, but must infer their place of origin from their energies and composition. For the highest-energy cosmic rays, although in theory it should be possible to trace them back to their origin, their rate of detection is so low that there is no discernible stream of particles coming from any one particular direction.

Detecting cosmic rays is, for the most part, a non-trivial exercise. The Earth's atmosphere is largely opaque to cosmic rays meaning that spaced-based detectors are required. This works well for the abundant low-energy cosmic rays, but due to the necessarily small size of the detector, the chance of detecting a much rarer, high-energy cosmic ray is very remote.

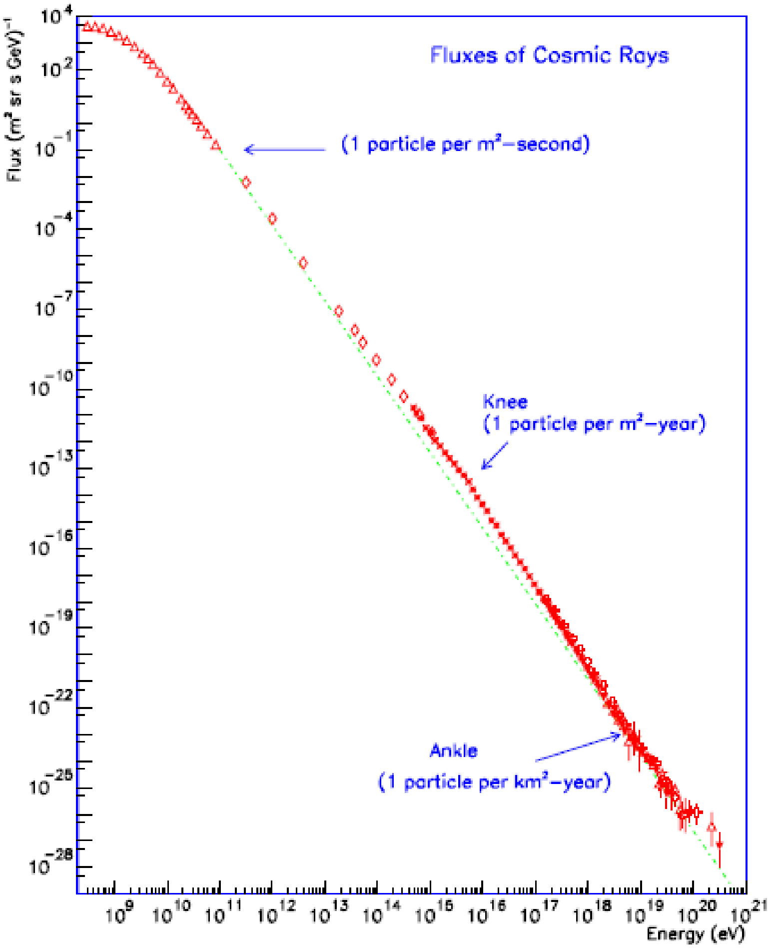

Figure 2.1 The cosmic ray spectrum measured at the top of the atmosphere. Above the energy of 10^9 eV the spectrum shows a power-law behavior. There is a change in slope at the knee (4×10^{15} eV) and at the ankle (5×10^{18} eV). The integrated flux above the ankle is about 1 cosmic ray per km^2 year.

Fortunately, cosmic rays with energies greater than $\sim 10^{14}$ eV can be indirectly detected from the ground. When they enter the Earth's atmosphere these cosmic rays interact with atoms to produce secondary particles in a cosmic ray shower. It is then possible to determine the energy and direction of the original cosmic ray by studying the shower of particles.

Cosmic rays were discovered in 1912 by Victor Hess, an Austrian physicist who took an ionization chamber (a device which detects charged particles) up into the Earth's atmosphere in a balloon. As the balloon rose he found that the numbers of charged particles initially dropped off, easily explained if these particles came from the Earth. Then, surprisingly, the numbers of charged particles began to rise again. He concluded that these charged particles were coming from outside the Earth's atmosphere and named them cosmic rays. In 1936 he was awarded the Nobel Prize in physics for this work.

These days, based on their energies and composition, astronomers divide cosmic rays into four main types: galactic cosmic rays, Solar Energetic Particle(Solar Particle Events), anomalous cosmic rays and ultra-high energy cosmic rays. These divisions are our best guess at classifying different types of cosmic rays given the information we have at the moment, and may be confirmed or revised with the next generation of cosmic ray detectors currently in development.

2.1.1 Galactic cosmic rays

Galactic cosmic rays (GCRs) are fully ionized atomic nuclei and other sub-atomic particles emitted by energetic sources outside of the solar system such as stars and highly energetic objects such as supernovae. GCR of $Z > 26$ are produced and accelerated by shock waves from supernovae. The abundance of GCRs by Z reflects the cosmic abundance of elements. By far the most abundant component is hydrogen nuclei or protons (numerically about 85%) followed by helium nuclei (about 13%) followed by other elements up to iron ($Z = 26$) with even-numbered elements such as ^{12}C, ^{16}O and ^{28}Si being more abundant than odd-numbered elements (Mewaldt, 1988).

Recent GCR composition data in several energy bands is available at the project website of the Advanced Composition Explorer (ACE) satellite which orbits about 1.53×10^6 km sunward of Earth, near the gravitationally-stable L1 Lagrange point (ACES, 2015). Data for selected particles at 200 MeV/n in 2007 from ACE along with earlier data for 1 GeV/n (Mewaldt, 1988) from the Interplanetary Monitoring Platform (IMP) satellite are shown in Table 2.1. Both data sets are from solar minimum periods (see below) and the two energy bins span the energy range associated with the maximum fluence in the GCR energy distribution. The selected particles represent those most widely used in radiobiological investigations.

Table 2.1 Galactic cosmic ray composition for selected elements commonly used in NASA sponsored accelerator experiments.

GCR composition for selected ions		Cycle 21/22 minimum (Mewaldt, 1988)		Cycle 23/24 minimum (ACES, 2015)	
Z	**Element**	**1 GeV/n**		**200 MeV/n**	
1	H	3,000	91.092%	1,660	85.531%
2	He	270	8.198%	256	13.190%
6	C	6.40	0.194%	7.45	0.384%
8	O	5.93	0.180%	7.16	0.369%
14	Si	1.00	0.030%	1.00	0.052%
22	Ti	0.08	0.002%	0.10	0.005%
26	Fe	0.59	0.018%	0.65	0.033%

The energy spectrum of GCR ranges from <1 keV/n to over 10^5 MeV/n. Their median energy inside the solar system is $\approx$1,000 MeV/n. For convenience, GCRs of energy < 30 MeV/n are often neglected in descriptions of space radiation environments because their ranges are so small that they would not pass through typical shielding levels. In the energy range from 1 to $\approx$ 1,500 MeV/n (accessible in particle accelerator facilities), the particle abundance rises to a local maximum at $\approx$ 200–800 MeV/n followed by an exponential decline as shown in Figure 2.2. Galactic cosmic rays are isotropic in terms of direction and are steered by magnetic fields. The fluence and spectra of GCRs are under constant surveillance by many orbiting satellites and measurements have been obtained to distances beyond Pluto to the boundary of the heliosphere at $\approx$ 90– 160 astronomical units (au; the average distance from Sun to Earth or 149,597,871 km) (NCRP, 2006). The IMP and ACE satellites have generated the most comprehensive data sets for interplanetary magnetic fields and charged particles. GCR composition is found to be only weakly dependent on distance from the Sun (Mewaldt, 1988). The GCR fluence and energy spectrum are modulated by solar activity corresponding to the 11-year solar cycle. At solar maximum, the enhanced emission of solar wind and altered heliospheric magnetic field serve as a barrier to GCRs such that overall fluences are reduced; fluences of lower energy particle are reduced by over an order of magnitude (Fig. 2.2).

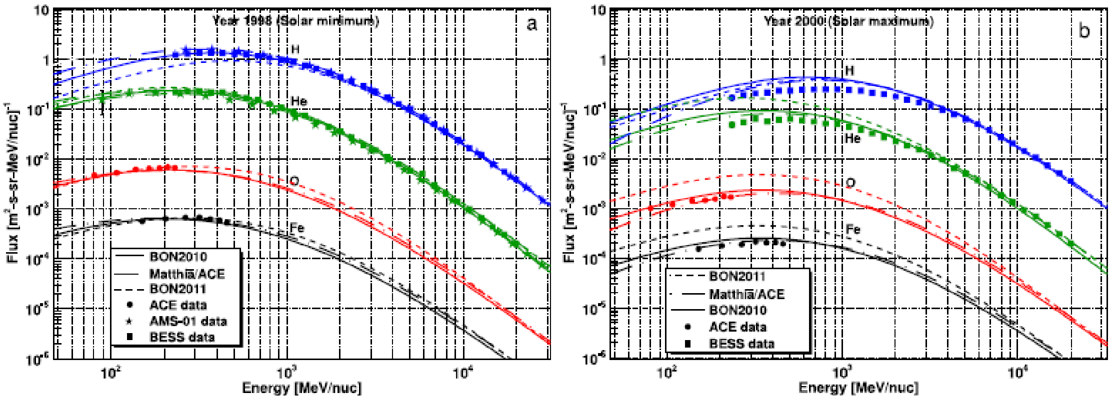

Figure 2.2 Comparison of GCR hydrogen (blue lines), helium (green lines), oxygen (red lines) and iron (black lines) energy spectra described by BON2011 (dashed lines), BON2010 (continuous lines) and Matthiä/ACE (dashed-dotted lines) models with measurements from various measurements: BESS (solid square symbols), AMS-01 (solid star symbols) and ACE/CRIS (solid circle symbols) for solar minimum (June-July 1998) and solar maximum periods (August 2000).

Source: Alankrita (2013)

2.1.2 Solar particle events

The Sun also contribute to the ionizing radiation. This radiation is due to Solar Particle Events (SPEs) or Solar Energetic Particles (SEPs). The energies of the SEPs are in average lower than energies of GCR particles but they are more abundant. The charged SPE particles are accelerated into the interplanetary space following mass ejections from the Sun corona. SPEs occur at unpredictable times. There is a correlation between SPE and the number of sunspots and thus the Sun activity (Ballarini, 2006). SPEs occur about 5 to 10 times per year (except during solar minimum). It is hard to predict the exact onset time. It is only possible to tell whether a large or small SPE has occur many hours after the event (Cucinotta, 2012). Figure 2.3 illustrates proton fluence (in protons/cm^2) of large SPEs with energies E>30, >60, and >100 MeV. Notice how the fluence of less energetic protons is higher than the fluence of higher energetic protons.

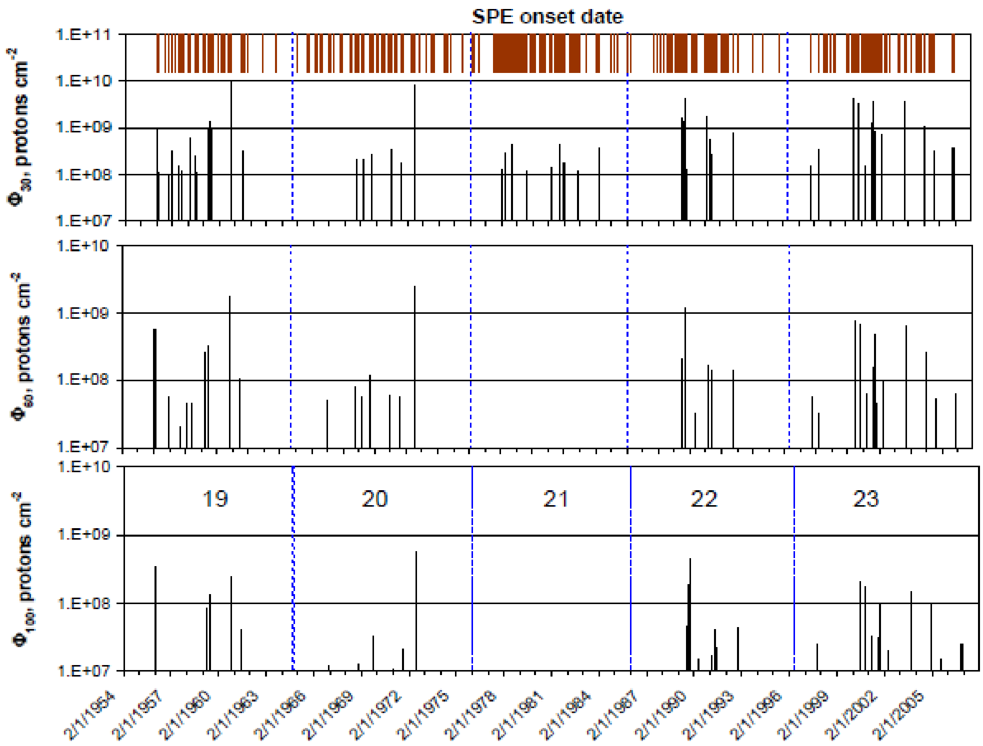

Figure 2.3 Large SPEs (proton fluence at E>30, >60 and >100 MeV) as a function of time.

Source: Kim (2012)

Like GCRs, SPEs primarily consist of protons but also include alpha particles and heavy ions with a composition that varies from event to event (Adams, 2005). Protons have energies in the range of 1keV to 1000 MeV but the main part of the spectra is below 200 MeV/n; this is shown in figure 2.4. Some SPEs can reach a fluence of more than 10^{10} particles/cm^2, which happens in the timeframe from few hours to several days. For example, SPE of the August 1972 was potentially lethal for a human crew on the Moon surface without appropriate shielding (Ballarini, 2006). While the average particle energy for SEPs is lower than for GCRs, the flux is much higher (Adams, 2005).

The Sun's activity not only drives SPEs but also affects the intensity of GCR. During their travel from the Sun, energetic particles interact with Galactic cosmic rays. This lead to reduction in the cosmic ray intensity, known as the Forbush Decrease (FDs). Decrease in intensity is followed by a slower recovery on a time scale of several days (Belov, 2014). SPEs are strong enough to affect GCR particle with energies less than

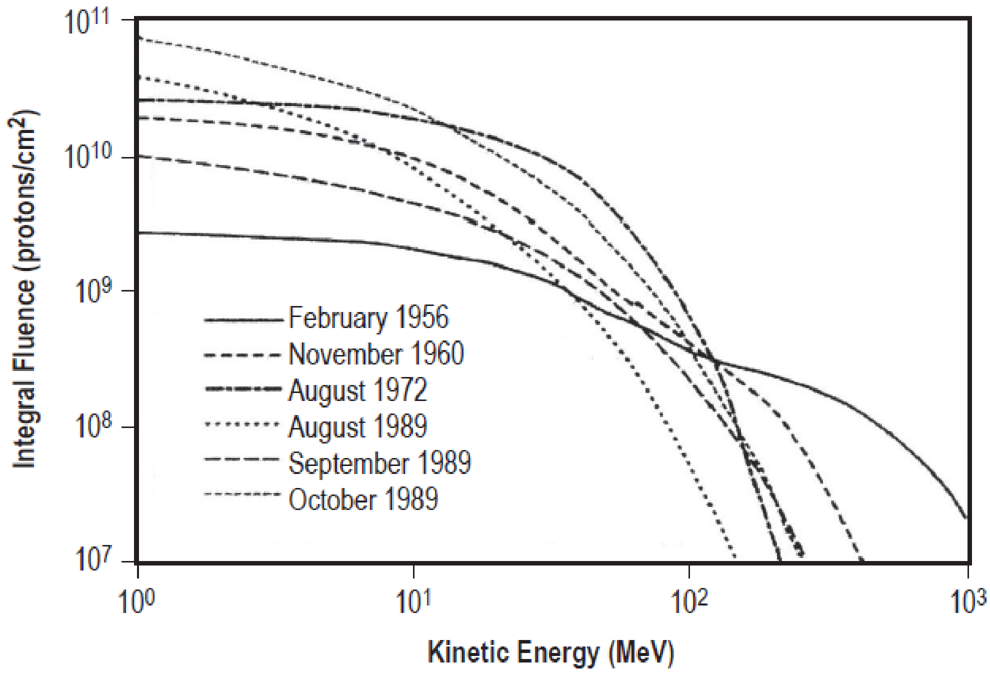

Figure 2.4 Spectra of larger solar particle events from 1956 to 1990.

Source: Shea (1990) and Sauer (1990)

about 2000 Mev/amu, which are modulated by the 11-year solar cycle. The GCR intensity can drop by more than a factor of two during a solar maximum compared to a solar minimum when solar wind is the weakest (Cucinotta, 2012).

2.1.3 Anomalous cosmic rays

Anomalous Cosmic Rays (ACR) were discovered due to the striking anomalies in the low energy quiet time spectra of He, N, and O (Garcia-Munoz et al., 1973, Hovestadt et al., 1973, McDonaldet al., 1974). These spectra showed for example a He/H ratio > 1 at E < 30 MeV/nuc and a C/O ratio < 0.1 at -10 MeV/nuc, not compatible with solar and galactic cosmic ray (GCR) abundances. This led to the name “anomalous”cosmic rays. Subsequently the elements Ne (von Rosenvinge and McDonald, 1975, Klecker et al. 1977), Ar, small amounts of carbon (C/O - 1%, Cummings and Stone, 1987), and H (Christian et al., 1988) have been detected in this ACR component. The apparent overabundance of elements with large first ionization potential led to the hypothesis that the ACR component originates from interstellar neutral particles that penetrate into the inner heliosphere, are ionized by solar UV and by charge exchange with solar wind ions, are then convected into the outer heliosphere, and are accelerated there to energies of 10 to -

100 MeV/nuc (Fisk et al. 1974), presumably at the solar wind termination shock (Pesses et al. 1981, Jokipii, 1986). Being predominantly singly ionized, these ions would be much less modulated than the fully ionized galactic cosmic rays or highly charged solar cosmic rays of the same velocity and thus could be observed in the inner heliosphere. This model provided a qualitative explanation of the ACR component and much effort in the last 25 years was devoted to delineate the observed properties and better understand the physical processes involved: The penetration of interstellar neutrals into the heliosphere, The ionization (pickup) of neutral particles in the solar wind, The particle losses due to charge exchange reactions and energy loss by adiabatic deceleration, The acceleration of pickup ions from - 1-10 keV/nuc to > 10 MeV/nuc, and The transport back into the inner heliosphere.

It is now generally agreed that the ACR component includes H, He, N, O, Ne, Ar, and small abundances of C. A comprehensive set of ACR spectra from several spacecraft in the inner and outer heliosphere has been compiled recently (Marsden et al., 1998). New measurements in the inner heliosphere at 1 AU with advanced instrumentation of high sensitivity on the WIND and Geotail spacecraft show evidence for an ACR-type enhancement in the low-energy spectra of S (Reames et al., 1997, Takashima et al., 1997). Measurements from Voyager-1 and -2 in the outer heliosphere at - 68 and - 58 AU, respectively, indicate low energy enhancements of Si, S, and Fe (Stone and Cummings, 1997). These new candidates of ACR elements have rather low first ionization potentials (10.36 eV (S), 8.15 eV (Si), and 7.87 (Fe)), i.e. they are expected to be predominantly ionized in the interstellar medium and thus were originally not thought to contribute to the ACR population. Whether the source of these elements are indeed interstellar neutrals or whether their origin is in the heliosphere needs further investigation.

2.1.4 Ultra-high energy cosmic rays

Ultra-high energy cosmic rays (UHECRs) are extremely energetic subatomic particles (mostly protons, but also some heavier atomic nuclei) with energies greater than 10^{17} eV (M.T. Dova, 2015). The record holder so far is a UHECR with an energy of 3×10^{20}eV equivalent to a baseball thrown at 160 km/hr.

Currently it is only possible to observe UHECRs through the cosmic ray showers produced as they interact with the Earth's atmosphere. This indirect method of observation is required due to the extremely low numbers of incident cosmic rays at these energies. The most advanced ground-based experiments to detect cosmic ray showers extend over several kilometers and consist of both Cherenkov detectors monitoring several large tanks of water for light produced by high-energy particles, and fluorescence detectors used to track the glow of the particle as it descends through the atmosphere.

The source of UHECRs remains a mystery, as does the mechanism to accelerate particles to these energies. However, they have enough energy to escape the typical magnetic field of a spiral galaxy, and most astronomers believe that UHECRs are of extragalactic origin. Possible sources include active galactic nuclei, dormant quasars with associated supermassive black holes and galaxy mergers.

Even if UHECRs are created in extreme extragalactic environments, it is still not clear how we are able to detect them at such high energies. Above 5×10^{19} eV, cosmic rays should interact with the radiation of the cosmic microwave background within a distance of 150 million light years, a process that should reduce the cosmic ray's energy below this threshold. This theoretical upper limit to the energy of a cosmic ray is called the Greisen-Zatsepin-Kuzmin limit (GZK limit) (Greisen, Zatsepin and Kuz'min, 1966), and the fact that we observe cosmic rays at energies larger than this appears to contradict the predictions of special relativity.

Although several exotic theories have been advanced to resolve this issue, other less-radical solutions have also been proposed: The detections were due to instrumental error or misinterpreted data, UHECRs have a local origin and UHECRs are weakly interacting particles.

It is hoped that the new generation of cosmic ray experiments will unequivocally verify or refute earlier measurements of energies greater than the GZK limit, and determine whether such extreme cosmic rays do indeed exist.

2.2 Basic concepts of radiation

Table 2.2 summarizes a few important quantities used in this paper. Radiation exposure is defined by the physical quantity called absorbed dose, D. It describes how much energy is absorbed by a unit mass. The units of absorbed dose are Joules/kg or Gray (Gy). An old equivalent to this unit is Roentgen, R, which had units of rad.

To quantify the health effect from the given amount of absorbed dose, a special quantity called Dose Equivalent is used. This is just dose absorbed, D multiplied by a scaling parameter called radiation quality factor, Q. Its units are called Sievert. The number of particles per unit area is called Fluence, F. It has units of $1/cm^3$. When particles pass through matter they lose energy at a certain rate, which depends on their kinetic energy and the charge-to-mass ratio of the material they traverse (Z/A). This rate has a special name – Linear Energy Transfer, LET. It has units of keV/ µm. The relationship between dose fluence and LET is $D=F/\rho \cdot LET$, where ρ is density of the material.

Table 2.2 Important radiation quantities

Quantity	Definition	Notation	Units (new)	Units (old)	Conversion
Exposure	Charge per unit mass	-	-	Roentgen (R)	1 R = 2.58×10^{-4} C/kg
Absorbed Dose	absorbed energy by unit mass	D	Gray (Gy)	Radiation Absorbed Dose (rad)	1 Gy = 1 J/kg 1 Gy = 100 rad
Dose Equivalent	Biological effect from absorbed dose	H	Sievert (Sv)	Roentgen Equivalent in Man(rem)	1 Sv = 100 rem
Fluence	# of particles per unit area	F	$1/cm^3$	-	-
Linear Energy Transfer	Rate of energy loss	LET	keV/µm	-	$D=F\cdot LET/\rho$
Fluence Spectra	Spectra of particles-to-energy range relationship	$\varphi_j(E)$	$1/cm^3$ over MeV/amu	-	-

As mentioned above, cosmic rays have a very broad energy range. Oftentimes it is useful to see how the abundance of specific type of particles spreads over this range. Figure 2.2 shows such spread for hydrogen, helium, oxygen and iron particles. Note that the energy range is given by energy per nucleon. This energy spectrum is denoted as fluence spectrum, $\varphi_j(E)$, where subscript j refers to the particle type described by atomic and mass numbers (Cucinotta, 2012).

2.3 Flux types

Both the GCR and SPE spectra are measured in terms of intensities of corpuscular radiation with various units that depend on detection method (Jursa, 1985). Intensity is a function of energy, time, steradians and area so it can get quite confusing. Usually there are two ways to specify intensity. The differential intensity, $J(E)$ is the number of particles per unit time of a given energy within certain energy interval incident on a unit area perpendicular to the direction of observation. It has units of #/cm^2/s/sr/MeV. Another way to describe intensity is with quantity called integral intensity, $J(>E)$. The $>E$ means that the intensity is measured only for those particles whose energy is greater than the threshold energy. Integral intensity is just the differential intensity integrated over energy:

$$J(>E) = \int_E^\infty J(E)dE \tag{2.1}$$

It has units of #/cm^2/s/sr (Jursa, 1985). To complicate things even farther, since both J and $J(>E)$ contain steradians units, they are called *unidirectional* differential and integral intensities respectively. If unidirectional intensities are integrated over 4π steradians solid angle, they are called *omnidirectional* differential and integral intensities respectively:

$$J_\Omega = \int_0^{4\pi} J(\Omega)d\Omega \tag{2.2}$$

where Ω is solid angle. Usually the term intensity is interchangeably used with the terms flux, (J) or fluence (Φ). The difference between them is somewhat ambiguous. While in one source a flux is defined as a derivative of fluence with respect to solid angle, other sources express flux as a time rate of change of the fluence:

$$J = \frac{d\Phi}{d\Omega} \tag{2.3}$$

$$J = \frac{d\Phi}{dt} \tag{2.4}$$

Using the first definition, a flux is the unidirectional intensity while fluence is omnidirectional intensity. Table 2.3 clarifies the complexity of these definitions.

Table 2.3 Difference between unidirectional and omnidirectional

with or without directional units	intensity type	unit
unidirectional (flux)	differentia	#/cm^2/s/sr/MeV
	integral	#/cm^2/s/sr
omnidirectional (fluence)	differentia	#/cm^2/s/MeV
	integral	#/cm^2/s

In this study all the SPE spectra are given as omnidirectional fluences (usually differential) while the GCR spectra is given as an unidirectional flux because that is convention in the literature.

The plot of the differential or integral intensities versus energy is the most common way to depict the radiation flux of the GCRs and SPEs. Sometimes, instead of energy, the flux spectrum is given in terms of magnetic rigidity, R that is a measure of a particle's resistance to a magnetic force that deflects it from a straight-line trajectory. These plots are usually reported by earth-based observatories because they measure particles with magnetic rigidity high enough to get through the "filter" of the earth magnetic field(Jursa, 1985).

2.4 Spectral models

Sometimes, often during solar maximum, SPE fluences become extremely large. Such SPEs, called Ground Level Enhancements (GLEs), are of particular interest because of the acute radiation exposure they can cause to humans and electronics. GLE events are measured in terms of integral fluence. It is relatively easy to do. All it takes is to count the number of particles with each energy that hit a detector. Once the experimental data are collected, the spectrum must be determined by deriving a mathematical expression that has a good fit with the data acquired by observation. Today, scientific community uses three spectral models.

2.4.1 Exponential model

The first method is exponential in proton rigidity fit (EXP) developed by W.R. Webber et al back in 1963. This method is an exponential function based on two proton integral data points at 30 and 100 MeV. Beyond 100 MeV the particle energy spectrum is extrapolated to 1 GeV. As name suggest, EXP is a function of particle's rigidity, not energy:

$$\Phi(>E) = N_0 exp(-R/R_0) \tag{2.5}$$

where $\Phi(>E)$ is the integral energy fluence in protons/cm^2. N_0 is a normalization constant, R – proton rigidity in MV (10^6 volts) and R_0– characteristic rigidity in MV. The conversion from rigidity to energy in MeV is as follows:

$$R = A/Z\sqrt{E^2 + 2E_{0A}E} \tag{2.6}$$

where A is atomic mass number, Z is atomic number, E_{0A} is rest mass energy (Atwell, 2011, Jursa, 1985). It is a usual practice to consider protons as the only constituent of SPE spectra. Therefore, A, Z and $E_{0A}$are values for proton. EXP method was used for several decades until a new methodology was introduced.

2.4.2 Weibull model

The second spectral fitting method is called Weibull fit, which is also an exponential function but unlike EXP it is exponential in energy:

$$\Phi = \Phi_0 exp(-kE^{\alpha}) \tag{2.7}$$

where Φ can be either the proton fluence or the proton flux having energy that exceeds a threshold energy E (Xapsos, 2000). Xapsos takes the units of Φ to be cm^{-2} when it represent integral fluence and cm^{-2}s^{-1}sr^{-1}when it represents integral flux (see table 2.3). Three constants Φ_0 , k and α are "Weibull" nonlinear regression fit parameters which are unique to each SPE. Φ_0 is related to the event magnitude while k and α are related to the spectrum hardness. The calculation method of these parameters is beyond the scope of this study and only parameters for notable solar events were adopted from the Xapsos paper and are listed in Table 2.4 . The function is fitted to the maximum energy value of 1 GeV (Xapsos, 2000).

Table 2.4 Weibull fit parameters for some SPEs.

Onset Date	Φ_0 (cm^{-2})	k (MeV^{-1})	α (cm^{-2}s^{-1}sr^{-1})
4 Aug, 1972	2.455$\times$10^{10}	0.0236	1.1080
12 Aug, 1989	1.622$\times$10^{11}	1.1660	0.4015
29 Sep, 1989	3.631$\times$10^{10}	0.8770	0.3841
19 Oct, 1989	1.230$\times$10^{12}	2.1150	0.2815
23 Mar, 1991	1.660$\times$10^{11}	0.9720	0.4410

2.4.3 Band function model

Finally, the third spectral model is called a Band function, which is a double power law in proton rigidity. The distinctive feature of this function is that it completely describes the entire proton energy spectrum. The method is based on the actual proton data observed in the range of medium to high energies (10 to several hundred MeV). The proton spectrum at higher energies is deduced from the secondary neutrons produced by SPE protons colliding with the Earth's atmosphere, which are registered by high latitude neutron-monitor stations. This method is a function of proton rigidity. The integral fluence is broken into two parts depending on the proton's rigidity:

$$J(>R) = J_0 R^{-\gamma_1} e^{-R/R_0} \qquad \text{if} \quad R \leq (\gamma_2 - \gamma_1) R_0 \tag{2.8}$$

$$J(>R) = J_0 R^{-\gamma_2} [(\gamma_2 - \gamma_1) R_0]^{\gamma_2 - \gamma_1} \cdot e^{\gamma_1 - \gamma_2} \qquad \text{if} \quad R \geq (\gamma_2 - \gamma_1) R_0 \tag{2.9}$$

where $J(> R)$ is the integral fluence (particles/cm^2), J_0 is the normalization constant, R$_o$ is the characteristic rigidity (GV) and γ_1 and γ_2 are spectral indices. The Band Fit parameters for several SPE events are included in Table 2.5 (Tylka, 2010).

Table 2.5 Band fit parameters for some SPEs.

GLE's Date	Official No.	$J_0(p/cm^2)$	γ_1	γ_2	$R_0(GV)$
1956 Feb 23	5	8.19E+08	0.584	5.04	0.3207
1960 May 4	8	8.16E+05	1.527	4.88	0.5850
1989 Oct 19	43a	1.22E+09	0.528	5.81	0.1621
1989 Oct 19	43b	9.09E+09	0.911	4.43	0.0844
1989 Oct 22	44	1.09E+09	1.226	7.25	0.1352
1989 Oct 24	45	4.42E+07	2.176	5.65	0.3850
1990 May 28	50	7.66E+07	0.417	4.98	0.1433
2005 Jan 20	69	3.80E+08	0.719	5.78	0.2040

This method was successfully applied to about 70 GLE events that occurred after 1956. The Band function is a strong candidate for being the best method used for future GLE assessment and analysis (Atwell, 2011).

2.5 Exposure levels and risk estimation

Galactic cosmic ray ions are able to penetrate several tens of centimeters of materials such as aluminum or tissue (water) and nuclear interaction between GCR particles and target nuclei will produce lower Z secondary particles whose lower LETs confer greater range than the primary particles. As a consequence, practical levels of shielding materials will not fully absorb all space radiation, and there will be unavoidable exposures to be kept to a minimum. NASA has estimated that exposures will result in each of an astronaut's cells (assuming $\approx$100 μ m^2 projected area or geometric cross section) being "hit" (traversed) by a proton once every three days, a helium nucleus once every few weeks and a heavy ion (Z > 2) once every few months (Nasa, 2015). The particle spectrum and fluence rates will result in deepspace tissue dose- and dose-equivalent rates of around 0.3–0.6 mGy/day and 1–1.8 mSv/day, respectively; these estimates have been directly verified by the Mars Science Laboratory spacecraft (Zeitlin, 2013). However, the long track ranges mean that very large numbers of cells in cylindrical volumes around the tracks will be simultaneously traversed, so that the "hit" kinetics are nonrandom and functional units of multiple cells may not respond independently. NASA has estimated exposure levels for a set of design reference missions that are engineering-based overviews of conceptual missions and include destinations in cis-lunar space, lunar surface outposts, asteroids, as well as Mars and its moons (2014). They take into account location in space, mission duration, operations and vehicle design and shielding. Sophisticated computer simulations (radiation transport codes) then utilize space radiation environment models (Badavi, 2014, 2014, Mrigakshi, 2013) to project mission exposures to the interior of vehicles. Computerized anatomical models of human bodies further enable exposure estimates for organs and tissues. Finally, radiobiological and epidemiological data and models are used to estimate adverse consequences of exposures. This information has been synthesized by expert panels into recommendations for spaceflight agencies to aid in estimating health risks and identifying mitigation or countermeasure strategies (Dietze, 2013, 2006, 2000). Current exposure estimates by NASA for different reference missions assuming 10 g/cm^2 shielding and ICRP 60 quality factors (1991) are as follows:

(1) low-Earth orbit 6–12 months, 50–100 mSv (1/3 from protons and 2/3 from GCRs);

(2) deep-space sortie – 1 month, 32.1 mGy/Eq with 16.7 mGy from GCRs;

(3) lunar visit/habitat, 231 mGy/Eq with 120–150 mGy from GCRs;

(4) deep-space journey – 1 year: 385 mGy/Eq with 200 mGy from GCRs; and

(5) Mars mission at solar minimum (approximately 3 years), 1.0–1.2 Sv (245–360 mGy) comprised of 130–180 mGy protons, 45–70 mGy He, 20–40 mGy $3 < Z < 9$ particles, 30–40 mGy $Z > 10$ particles and 20–30 mGy neutrons and other particles.

These estimates incorporate many assumptions and are constantly updated and revised. NASA has identified four major categories of risk from space radiation exposure. These are: 1) carcinogenesis; 2) degenerative tissue risk (e.g., cardiovascular disease); 3) acute (during a mission) and late (after a mission) risks to the central nervous system (CNS); and 4) acute radiation syndromes. Research activities for these risks are related to a codified set of research questions (2015). Perhaps the best developed risk model for space radiation is NASA's NSCR 2012 model for cancer risks that projects cancer incidence and mortality incorporating mission design parameters, epidemiological data, radiation fields, dose rates and quality factors, and establishes a probability distribution for risk of exposure-induced death that enables estimates of uncertainty (Cucinott, 2013). NASA establishes a cancer exposure limit such that “planned career exposure to ionizing radiation shall not exceed 3 percent Risk of Exposure-Induced Death (REID) for cancer mortality at a 95 percent confidence level ”(Nasa, 2007). The many components of uncertainty are dominated by biological issues such as quality factors, dose-rate effectiveness factors, rules for combining effects from multiple ion types and their order of exposure and modifying effects of other spaceflight environmental features such as low gravity, confinement and isolation stress, sleep deprivation, etc. For noncancer risks, permissible exposure limits (PELs) for short-term and career exposures to space radiation have been approved by NASA and set requirements and standards for mission design and crew flight assignment. Current PELs are shown in Table 2.6 (Nasa, 2007). Because tissue-weighting factors are not well established for the CNS, values are given in Gy rather than Gy/Eq.

Table 2.6 Permissible exposure limits used by NASA to set requirements and standards for mission designs and crew flight assignments

Target organ	**Permissible exposure limits in Gy or Gy/Eq**		
	30-day exposure limit	**1-year exposure limit**	**Career exposure limit**
Lens	1.0 Gy/Eq	2.0 Gy/Eq	4.0 Gy/Eq
Skin	1.5 Gy/Eq	3.0 Gy/Eq	6.0 Gy/Eq
BFOs	0.25 Gy/Eq	0.50 Gy/Eq	No applicable
Heart	0.25 Gy/Eq	0.50 Gy/Eq	1.0 Gy/Eq
CNS	0.50 Gy	1.0 Gy	1.5 Gy
CNS ($Z \geq 10$)	Not specified	0.10 Gy	0.25 Gy

Note: CNS = central nervous system; BFOs = blood-forming organs.

Ground-based experiments with charged particles using appropriate biological models are critical in establishing dose responses, dose-rate effects and dependence on track structure. To date, most ground-based experiments have involved acute exposures to beams of single-energy accelerated ions. The NSRL at Brookhaven National Laboratory has been the focus of such studies in the U.S. since the late 1990s. It provides a series of beams from protons to iron ions with energies up to 1 GeV/n with an ongoing upgrade to 1.5 GeV/n for heavy ions (Lowenstein, 2007). Importantly, there are ongoing activities directed at extending experimental capabilities to simulate a multiple-ion GCR spectrum and to protract dose (Slaba, 2015, Kim, 2015). Although these simulations will be limited by accelerator facility operational capabilities, they will nevertheless allow researchers to simulate a mixed field in tissue that will be dominated by protons and helium ions along with selected heavy ions as would be found in the interior of spacecraft and human bodies due to radiation shielding and transport (Slaba, 2015). The contributions to exposure from neutrons are also considered in simulation models. While neutrons decay with a half life of about 10 min in free space they are produced abundantly by interactions of charged particles with thick shielding (Norbury, 2014).

2.6 Principals of high energy particle interaction with matter

An understanding of the interaction processes between radiation and the traversed medium is necessary for radiation detection, measurement, shielding studies, radiation transport calculations and the assessment of the radiation-related health risks. When GCRs traverse through matter, they interact with the constituting atoms and molecules through electromagnetic and nuclear forces. The interactions between GCR and a target, e.g. spacecraft, produces a large variety of secondary particles (e.g. gamma radiation, electrons, muons, neutrons, pions and secondary protons and heavy ions). Neutrons and secondary ions are especially crucial for space applications since they can deposit large energies into the medium. Other secondary particles like electrons and photons contribute only a small fraction to the total exposure; however, since these can travel to greater distances than heavier particles and deposit energy there, they can be of importance in radiation protection in space. In this section some of the relevant radiation-matter interaction processes for space radiation studies are discussed.

2.6.1 Electromagnetic Interactions

While traversing through matter charged particles exert long-range Coulomb forces on the electrons of the target atoms along their path and undergo inelastic scattering thereby suffering energy loss as they penetrate deeper inside. The energy lost is transferred to the orbital electrons, causing ionization or excitation of the target atoms. The laws of conservation of both energy and momentum are important for the formulation of the energy losses of radiation in matter. By following these laws, the maximum energy transfer, T$_{max}$, that occurs during a single head-on collision between the heavy ion projectile of mass M with velocity v and the orbital electrons of mass m_e at rest can be deduced. The relativistic expression for maximum energy transfer is (Turner, 2007)

$$T_{max} = \frac{2\gamma^2 m_e v^2}{1 + 2\gamma m_e/M + m_e^2/M^2} \tag{2.10}$$

with $\gamma = \dfrac{1}{\sqrt{1-\beta^2}}$ and $\beta = \dfrac{v}{c}$ If $M >> m_e$ then equation 2.10 reduces to

$$T_{max} \approx 2\gamma^2 m_e v^2 \approx 2\gamma^2 m_e v^2 \beta^2 \tag{2.11}$$

From equation 2.11 it can be deduced that when the projectile protons or heavy ions i interact with atomic electrons, they lose a very small fraction of their energy during a head-on single collision and are only slightly deflected. This kind of scattering is also known as Coulomb scattering. Thus they travel mostly in nearly straight lines continuously transferring a small fraction of their energy during each collision (cross section $\sigma_{i,coulomb} \approx 10^{-16}$cm^2) (NCRP 2002) with the electrons on their path. Occasionally these ions can get large-angle deflections when undergoing elastic collisions with atomic nuclei ($\sigma_{i,elastic} \approx 10^{-19}$cm^2) (NCRP 2002) and transfer energy to them leading them to recoil.

Furthermore, sometimes the orbital electrons may gain sufficient energy from the projectile so that they may leave the atom and induce secondary ionization of neighbouring atoms. Such electrons are often called δ-electrons or δ-rays. The range of δ-rays is small compared to the charged ions so that ionizations occur close to the primary ion track. However, sometimes they can be long-ranged and deposit energy at considerable distance from the primary ion track (Kobetich, 1968).

2.6.2 Stopping Power

A quantity described as the stopping power of a medium for a charged particle is used to determine the average energy loss per unit length in the medium and is of fundamental importance in radiation dosimetry (Leo, 1994). It is calculated as a product of the probability per unit path length, usually expressed in cm^{-1} of a charged particle to have an interaction and the average energy loss per collision usually expressed in MeV (Turner, 2007). The stopping power is thus usually given in MeV cm^{-1}. There are different kinds of stopping powers depending on the type of energy loss such as the collision stopping power (also known as electronic stopping power) and radiation stopping power. The former is associated with the inelastic collisions of the projectile ions with electrons which can lead to, e.g., ionization and excitation of target atoms and molecules. The latter is associated with the emission of bremsstrahlung photons when typically electrons, e.g., δ-rays are decelerated by sharp deflections caused by their interaction with atomic nuclei of the medium. Another type of stopping power is called the nuclear stopping power which is associated with the elastic collisions between the projectile ion and nuclei of the medium. It is only important for low energy heavy particles. When the projectile energy becomes higher, nuclear stopping is not important, and can be neglected in the calculations (Schiavi, 2003). The description of the collision stopping power is particularly important for the transport of ions in matter as they suffer energy losses mainly due to ionization as stated above. The expression for the collision stopping power of a uniform medium for relativistic heavy charged particles, $-dE/dx$, was derived from the work of Bohr (1913) and (1915), Bethe (1932), Bloch (1933) and is given by (Leo, 1994)

$$-\frac{dE}{dx} = 2\pi N_a r_e^2 m_e c^2 \rho \frac{Z}{A} \frac{z^2}{\beta^2} \left[\ln \left(\frac{2m_e \gamma^2 v^2 T_{max}}{I^2} \right) - 2\beta^2 \right] \tag{2.12}$$

where N_a is Avogadro's number , r_e is classical radius of electron z is charge of incoming particle, m_e is mass of electron Z is charge number of medium, A is mass number of medium ρ is density of medium, I is mean excitation potential of medium T_{max}, γ, β, v and c are the same as in equation 2.10

This formula is called the Bethe-Bloch formula (Leo, 1994) and is the basic expression for the energy loss calculations. For a complete description, certain correction factors associated with other processes that contribute to the energy loss of heavy charged particles have to be added in the equation 2.10. For example, the equation presented above has to be modified for energetic particles (energies in the GeV region and above). Other important corrections include the so-called shell and density corrections.

The shell correction accounts for the non-participation of the inner-shell electrons during ionization and excitation processes caused by low energy projectiles. The density correction considers the polarization of the atoms along the path of energetic projectiles wherein the distant electrons are shielded from the electric field resulting in lower contribution of the distant electrons to the total energy loss. See Leo (1994) for details regarding these correction factors and others that are not introduced here.

From the formula it is clear that the stopping power is dependent on certain properties of both the incident ion type, its energy and also on the target material. When particles have non-relativistic energy, their energy loss is dominated by $1/\beta^2$ term in equation 2.12. It follows from the equation that with decreasing velocity and energy of the projectile the energy loss increases. As a result, a characteristic maximum in the energy deposition with depth curve is observed at the end of their path in the medium and is called Bragg-peak. Another factor to note is that the energy loss of a particle is proportional to the square of their charge z^2. This means that heavier ions lose energy in a given medium at a faster rate than the lighter ones which further indicates that they have shorter range (penetration depth) as well. The equation also indicates the influence of the medium traversed on the energy loss of heavy ions. The energy loss is proportional to Z/A which means that materials having high charge-to-mass ratio, e.g. hydrogen in comparison with aluminium, will lead to greater energy loss of the projectiles.

Other processes leading to energy loss due to electromagnetic interactions are pair-production when high-energy particles on traversing through the Coulomb field of the target nucleus produce electron-positron pairs, and interaction of secondary photons with nuclei such as photoelectric effect and Compton scattering. In this chapter the interactions of photons with matter are not discussed. However, it has to be noted that photons, produced as secondaries by the incident heavy ions as in the case of GCRs, can be highly penetrating in a medium and can lead to energy deposition at a distance from their original locations.

2.6.3 Nuclear Interactions

Unlike the quasi-continuous energy loss through electromagnetic interactions of a charged particle along its track, the energy loss via strong interactions occur rather less frequently. This can be explained by the lower cross section of the strong interaction, i.e., $\sigma_{i,nuclear} \approx 10^{-24}$ cm^2, related to the size of the nucleus (radius $\approx 10^{-15}$ m) in comparison with the cross section for Coulomb scattering, $\sigma_{i,coulomb} \approx 10^{-16}$ cm^2 (radius of an atom $\approx 10^{-10}$ m). Additionally, the charged particles feel the repulsion from the nucleus thereby also leading to reduced probability for such interactions to occur. But when the energy of the ions are greater than what is required to overcome this repulsion, which is called Coulomb barrier, then these interactions can take place.

Nuclear interactions such as inelastic nucleus-nucleus or nucleon-nucleus interactions are dominant for heavy ions with energies above 100 MeV/nuc (Hüfner, 1985). These processes therefore are highly relevant for GCR nuclei interactions with the spacecraft and tissue. An important process at high energies called fragmentation can occur which leads to the production of secondary particles which further interact with the medium and lose energy. In such a process either the projectile or the target nucleus fragments (or disintegrates) into smaller nuclei and some nucleons (Hüfner, 1985). While the projectile fragments mostly preserve the velocity of the incident particle, the target fragments emitted are slow relative to the incident particle (Zeitlin 2012, NCRP 2006, Hüfner 1985).

The secondary neutrons are of great importance as they, being electrically neutral particles, are extremely penetrating and deposit large amounts of energy indirectly through the production of secondary charged particles due to nuclear interactions. If neutrons are produced with energies below $\sim$20 MeV, they may get absorbed by the nucleus leading to reactions such as the production of deuterium when a neutron is captured by a hydrogen atom (${}^{1}_{1}H(n,\gamma){}^{2}_{1}H$ reaction). This process, called radiative neutron capture, is accompanied by the emission of gamma rays which can in turn be absorbed by an atomic nucleus to knock out a nucleon. Other neutron capture processes can occur which may result in the emission of charged particles such as protons and alpha particles or induce nuclear fission (Turner, 2007). Another process that is associated with neutrons is evaporation which occurs when target nucleus may fragment due to high-energy neutrons (>100 MeV) which can lead them or the fragment nuclei to be in an excited state and subsequently decay while emitting nucleons including neutrons (Zeitlin, 2012). The fragmentation process during GCR interactions leads to a large production of pions. Some of these may decay or travel further to interact with target atoms and produce more pions, secondary nucleons, and photons. Thus pions also contribute to a significant amount of radiation exposure (Aghara, 2009).

The nuclear interactions of nuclei, especially heavy ions, are not yet described by any fundamental theory as these are not fully understood and the cross-sections are calculated using semi-empirical models in the transport codes (Zeitlin, 2012). NCRP (2006) and Zeitlin (2012) give a detailed description of nuclear interactions especially important to space radiation studies. For fragmentation process in particular, see Hüfner (1985).

2.6.4 Hadronic and Electromagnetic Showers

The cascade of secondary particle production as a result of interactions between high-energy particles with dense matter is often termed a shower. Thus, the interaction of GCR particles with spacecraft shielding and Earth's atmosphere mostly results in such showers. Hadronic showers are usually produced by high-energy nuclei, pions or atomic nuclei and can lead to electromagnetic showers due to the production of charged particles in the process. Electromagnetic showers are triggered by high-energy electrons via bremsstrahlung, or photons via pair-production which produce an electron-positron pair. Positrons may again recombine with electrons to emit more photons. This process continues to produce low energy photons and electrons which are ultimately absorbed by the atoms.

2.7 Shielding of Cosmic Rays

It is unlikely that the shielding approach can provide a technological solution that is feasible today because of the very high energies that GCR particles can reach and because of very high launch costs caused by increasing the amount of shielding material required for significant mitigation properties.

Materials with the smallest mean atomic mass are usually the most efficient shields for both SPEs and GCRs.When particles traverse a structural material, they interact with the nuclei of that material and therefore lose energy. Another consequence is a change in the composition of the radiation field or particle fluence. These changes in energy and fluence depends on the material that particles traverse. More specifically – the number of atoms per unit mass in the traversed material. The energy loss by ionization of a single component of shielding material with atomic number Z is proportional to the number of electrons per atom and thus proportional to Z/A, where A is the atomic mass number A of each element of the material. The energy lost per gram of material and per incident fluence (e.g., in units of particles per cm^2), the "mass stopping power," is also inversely proportional to the density, ρ (g/cm^2) of the material, so that the energy lost by one incident particle per cm^2 per unit mass is proportional to Z/(Aρ) (Cucinotta, 2012).

This ratio consists of two important components. The first component is Z/A ratio. It is proportional to the number of electrons per nucleon. Materials with small atomic mass have the highest number of electrons thus the ratio is higher. Hydrogen, for example, has the highest number of electrons per nucleus with Z/A ratio of 1.

The second component is density. The smaller the density, the higher the ratio. Therefore, the energy lost by energetic particle is higher for low density materials with small atomic mass numbers. Liquid hydrogen should be the most efficient material. Figure 2.5 shows values of Z/(Aρ) for different materials.

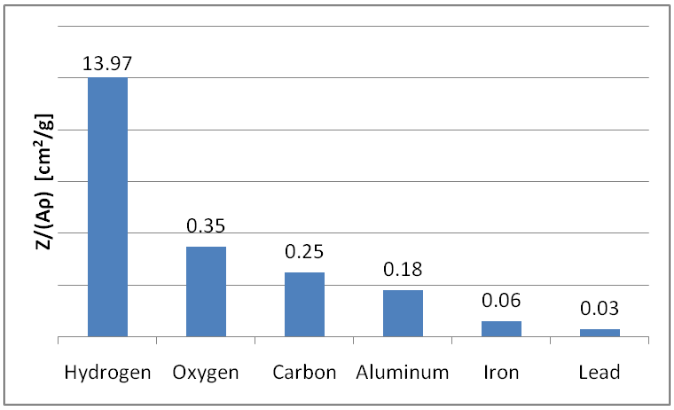

Figure 2.5 The Z/(Aρ) ratio values for different materials (hydrogen is in liquid form).

When an energetic particle interacts with an atom of the shielding material, both split into pieces producing secondary nuclei. These secondary particles are important in shielding considerations. Some elements break into neutrons while others, such as carbon, break into three α-particles. Although α-particles are much more biologically damaging, neutrons are of higher concern because of their longer ranges. Energetic particles lose their energy through ionization of target atoms. If this energy is greater than 1000 MeV/amu, ionization processes release electrons energetic enough to cause further ionization of nearby atoms and these electrons, having energies more than 1 MeV, are called δ-rays. The lateral spread of δ-rays is called track-width, which depends on velocity (energy) of the original particle and its atomic number according to the following ratio: $(Z/\beta)^2$, where β is the particle velocity scaled to the speed of light. Figure 2.6 clearly showing the increasing lateral spread of δ-rays along the track with increasing the charge Z. (Cucinotta, 2012)

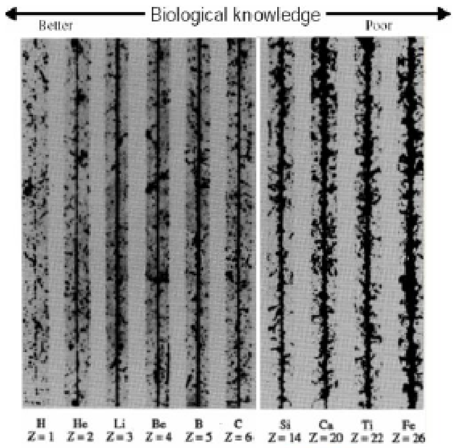

Figure 2.6 Different ions tracks in nuclear emulsion. Note the increase in number of δ-rays along the track with increasing atomic number.
Source: Cucinotta (2012)

On one hand, low-Z particles have a higher biological effectiveness. On the other hand, higher Z nuclei at the same LET (see table 2.2) affects more cell layers before it deposits all of it energy. To compare the biological effect of different particles types, a special term called Relative Biological Effectiveness, RBE is used. RBE is a ratio of doses causing identical effect. The numerator of this ratio is the dose due to well-studied gamma or X-rays and the denominator is the dose due to the particle being studied. RBE data is used to make estimates for human risk by defining a radiation quality factor. For terrestrial radiation exposures,quality factors, Q are determined uniquely by LET. For example, Q=1 corresponds to LET of 10 keV/μm while Q=30 corresponds to 100 keV/μm. This convention is not needed for space radiation environments and quality factors are then defined by E and Z instead of LET. Secondary particles, which are produced when primary particle traverse shielding material, can have quality factors higher than the primary particle. Figure 2.7 illustrates the dependence of the radiation quality factor for solid cancer on the primary particle's energy and Z. This figure illustrates the complexity of GCR interactions with matter. For example, consider a Fe particle with an energy of above 800 MeV/amu. While traversing through the shielding material, it loses energy, which can be illustrated by following the Fe curve from the right vertical line to the left. The quality factor in this case increases. If, on the other hand, the initial energy of the Fe particle is below 500 MeV/amu, the loss of energy causes quality factor to decrease.

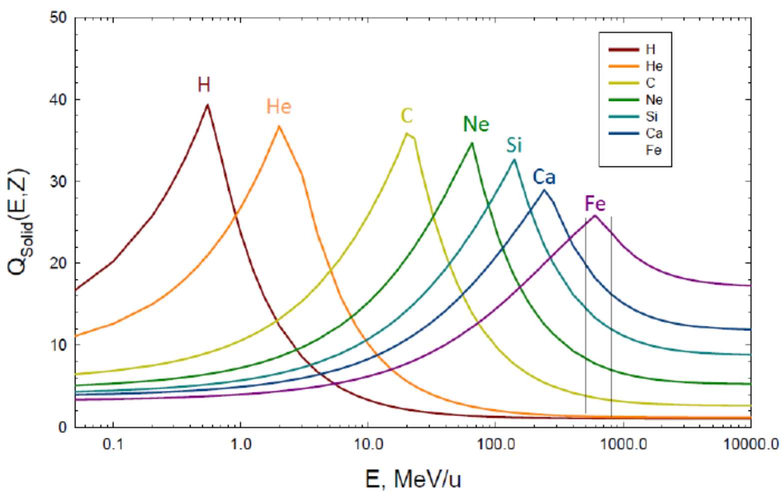

Figure 2.7 Dependence of the quality factor on a particle's energy for several GCR nuclei.

Source: Cucinotta (2012)

Another example that illustrates the complexity of the problem is a fragmentation of a Fe particle which creates new particles with lower Z and E as well as high energy neutrons, protons and other light particles. That increases population of the radiation field. Therefore, it is important to define particle flux spectra to evaluate effectiveness of shielding materials (Cucinotta, 2012).

CHAPTER 3
FLUKA: THE MONTE CARLO SIMULATION

To predict the effectiveness of shielding materials there are two options. The first, is to reproduce the radiation environment and make measurements behind the shield. Unfortunately, GCR particles can reach very high energies, even higher than the Large Hadron Collider – today the most powerful particle accelerator – can achieve not to mention the very high cost of using it anyway. Such high-energy ions, however, may have a noticeable contribution to the overall absorbed dose due to GCR. Therefore, it is impractical to reproduce the GCR environment in a laboratory on Earth and it is too expensive to perform such experiment in space every time a new shielding needs to be tested. The second option is to evaluate effectiveness of shielding materials by modeling the space radiation environment using a transport code. Such software is applied in many fields to design detectors, accelerator shielding, dosimetry, and many others. Transport codes characterize the modified radiation field downstream of the point of interaction between the incident radiation and the target nuclei. This characterization is in terms of absorbed dose or dose equivalent which is necessary to assess the response of electronics or, more importantly, biological systems (Aghara, 2015). Every transport code utilizes one of the two methods: analytic and probabilistic (Monte Carlo method). Analytic methods compute a mathematical function, which have a unique value for any input on its domain. Probabilistic or Monte Carlo (MC) methods rely on repeated random sampling to obtain numerical results. The histories of particle interactions are simulated using random numbers that model the probability of particle interactions.

One example of deterministic transport code is HZETRN developed by NASA Langley Research Center. A special online tool called OLTARIS is used to provide this code in a user-friendly environment. NASA engineers use this code to evaluate dosimetric information required to design space vehicles. It is based on one-dimensional formulation of the Boltzman transport equation (Wilson, 1997).

Examples of MC codes are MCNPX developed by Los Alamos National Laboratory, PHITS, developed by several institutes in Japan and Europe. Another example of a MC code is FLUKA. Since this code is used in this paper, it requires a bit more detailed introduction. FLUKA is a product of European Organization for Nuclear Research (CERN). This fully integrated Monte Carlo simulation package simulates particle transport and interactions with matter. Fluka's range of application is quite broad, spanning from accelerator shielding to dosimetry, radiotherapy and others. It can simulate interactions of about 60 different particles with the energies up to 20 TeV. The code can only be used with Linux and requires g77 compiler to build and run the user programs (Ferrari, 2005). The Fluka Advanced Interface (FLAIR) is a convenient graphical user interface to run FLUKA. It is an input file editor, which inspects the input syntax for errors and flags incorrect entries.(Figure 3.1)

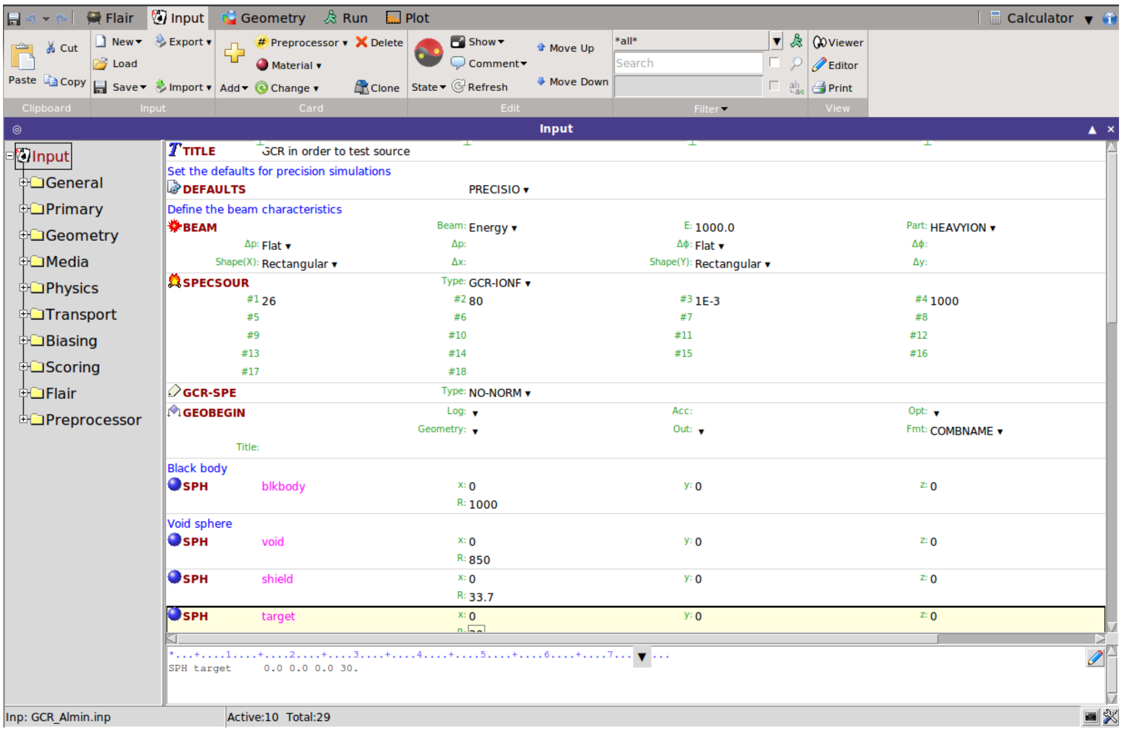

Figure 3.1 FLUKA input editing in GCR source with FLAIR, the fluka user interface.

3.1 How FLUKA works

FLUKA's input is a text file that has a list of option lines called cards. Cards consist of six numerical quantities (e.g. energy, coordinates, etc.) called WHATs where most of the information required for a card to serve its purpose is placed. Such information may be numerical data such as coefficients, energy ranges or dimensions. Every card belongs to a certain category. For example, category Geometry deals with the bodies and regions, Scoring contains detector cards and so on. Scoring cards need to be explained in more details because they are important for the further discussion. Each scoring card is designed to detect a specific quantity. The two cards used in this study are USRBDX and USRBIN. The first one defines a detector for a boundary crossing fluence estimator. It is used to score the differential fluence of the source and secondary particles in a shield. The output of this card is flux integrated over solid angle (omnidirectional) and has units of ions/cm^2/GeV/pr. The second scoring card, USRBIN, is used to score absorbed dose or dose rate. The output of this card is given in the units of GeV/g/pr. It describes how much energy was absorbed per unit primary weight (Ferrari, 2005). The fluka's output is always expressed "per primary particles" (hence the "pr" in the output units). The physical meaning of this primary varies with the type of source being simulated. In the case of a SPE source, the primary is a total fluence, sort of a normalization value that can be found analytically by calculating the area under the differential fluence and then employing the first fundamental theorem of calculus:

$$\text{primary is:} \qquad \Phi_{\text{total}} = \Phi(E_{\text{max}}) - \Phi(E_{\text{min}}) \tag{3.1}$$

where ϕ is the integral energy fluence in #/cm^2 (or primary/cm^2 for unit conversion purposes). The calculated primary is then applied to the output of both scoring cards: USRBIN and USRBDX. It will be shown further that, in the case of a GCR source, the physical meaning of a primary is related to time. Notice, however, that in the case of an SPE source, the units of both scoring cards does not contain time. Time doesn't show up at all in the case of SPE source while it does appear in the primary value when the source is a GCR. This is because, in the case of a SPE, the source is defined as an event which lasted and was recorded for a certain amount of time in the past. As a result, when the source is defined as SPE event, USRBIN detector measures absorbed dose instead of dose rate as in case of GCR source. This time span is embedded in the SPE source. FLUKA uses a special user routine code to read from the source file and to generate particles in the amount and of the energy specified in the source file. When these particles are incident on a scoring detector,the output of the detector card is always time independent because again the source is a finite event rather than a constant radiation background in the case of a GCR source while in a case of SPE, time is embedded in the primary value. Theoretically, both the source input and the fluence of the particles generated by fluka should be identical. This was checked and will be discussed farther in this paper. Also, the exact way a FLUKA source was created will be explained later.

When the source is defined as GCRs, the time does appear in the output. The GCR source, however, was not modeled as an event but rather as a continuous background radiation. Therefore, it is time dependent and, as mentioned earlier, the time unit of the scoring card is embedded in the normalization factor. However, this factor in the case of GCRs is defined differently than in the case of a SPE source. Instead of calculating the normalization factor from the source fluence, it can be found from the fluka output data. Fluka has a build in GCR package which not only generates a source for the fluka's run but also provides two values that are used to calculate the normalization factor and one of these values is time dependent. The GCR package is described later on.

Several input parameters affect the quality of the fluka output. One is the number of requested events also known as the number of source history particles in other codes. This parameter specifies how many particles are generated. More particles mean more points in the output, which makes the output more meaningful. However, a large value for this parameter comes with a price of a long FLUKA run, the greater the value, the longer the process. The second parameter is the number of runs. This value affects the output uncertainty. Obviously, the more times the same experiment is repeated, the smaller the statistical uncertainty (Ferrari, 2005). Figure 3.2 shows simulation process in FLUKA to calculate the absorbed dose from cosmic rays in this work.

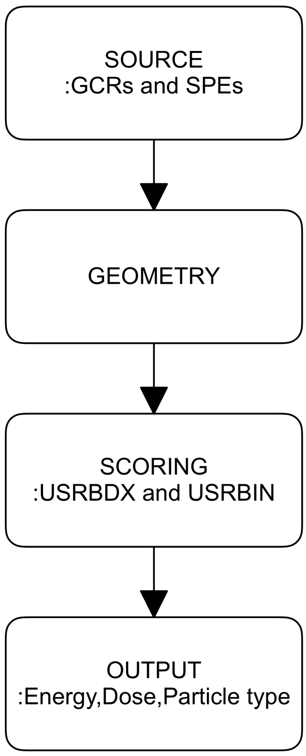

Figure 3.2 Diagram of simulation process in FLUKA to calculate the absorbed dose from cosmic rays in this work.

3.2 Source

Two source types were utilized for this study are GCRs and SPEs. The GCR source is a part of a package build into FLUKA. This package contains a model of the energy spectrum and composition of cosmic rays and the local interstellar medium. Ion composition of the galactic flux has been produced by the modified Badhwar code for various modulation parameters and written on 28 “.spc” files (Z+<PhiMV>+.spc). Each file corresponds to an element from Hydrogen to Nickel. There are two groups of 28 files:

(1) Solar minimum: <zzphi0465.spc>

(2) Solar maximum: <zzphi1440.spc >

Each file contains a differential flux in ions/cm^2/s/sr/(MeV/amu) with corresponding energy bin in MeV/amu, where sr is steradians and amu is atomic mass number. The spectrum is modified to follow recent data sets from the AMS and BESS experiments up to 100 GeV, according to the so-called ICRC2001fit (Sala).

To set up the GCR source in FLUKA, one specifies an energy interval and choose a starting radius (radius of the emission sphere in case of spherical geometry). The GCR package in FLUKA is designed mostly to model the interaction of energetic particles with Earth's atmosphere. All necessary normalization factors for different layers of the atmosphere are predefined. However, the purpose of this paper requires an interplanetary GCR source. Fortunately, all it takes to ignore these atmosphere-related normalization factors is to choose the "NO-NORM" in the GCR-SPE card. This way one obtains a raw GCR data without any kind of further normalization [18].Figure 3.3 shows the GCR fluence of four energetic particles used in GCR package.

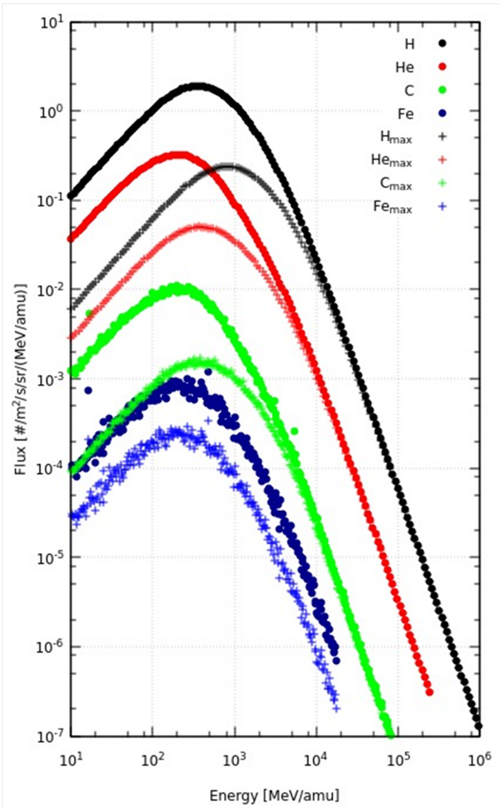

Figure 3.3 FLUKA's GCR source for proton spectrum, α-particles, carbon and iron ions in solar minimum and solar maximum.

3.3 SPE source verification

For the SPE source, There are not package build in. this study, was given as an ASCII (text) file containing energy data in discrete intervals with corresponding differential fluence values. This file is generated uising C++ code by vectorising differential form of one of the spectral fitting equations such as equations (2.5) - (2.9). The output of this code is an n×2 matrix where n is the number of discrete energy bins (usually 2000) and two columns are energy and differential fluence. FLUKA reads this file using a special user routine.

Before FLUKA can be used to study shielding characteristics of different materials, it is important to validate its results. This verification was performed by repeating a simple experiment described in a published and peer reviewed paper and by comparing results. The following is the description of main elements of FLUKA setup: the source of SPEs.

The paper used in this study was written by S.K. Aghara et.al (Aghara, 2015). This paper investigates the impact of several SPE fluxes . The simulation was performed by three transport codes: MCNPX, PHITS and OLTARIS. This paper reports result that are of main interest for the purpose of FLUKA validation: fluence spectra of four SPE events The same setup used in this paper was repeated with FLUKA.

The source in Aghara paper are four historically significant SPE events that occured in Feb 1956, Aug 1972, Oct 1989 and Mar 1991. Two things should be clearly defined before an SPE source is simulated by a transport code:

(1) the function form (integral or differential fluence)

(2) particular fitting function (EXP, Weibull or Band)

All events in this experiment were modeled only as proton fluence. The first event in the Aghara paper is called 56 Webber after W. R. Webber who used the EXP method, eq (2.5), to model the spectrum of this event back in 1963. The proton intensity is given in the differential form:

$$\frac{d\Phi}{dE} = 1.09 \times 10^{8} \frac{E + 938}{\sqrt{E(E + 1876)}} e^{\left(-\frac{\sqrt{E(E+1876)}}{100}\right)} \tag{3.2}$$

Note that this expression is obtained from eq.(2.5) by expressing rigidity in terms of energy according to eq.(2.6) and differentiating with respect to energy with N_0= 1.09×10^{10} and R_0= 100. It is not clear which fitting model was used for the 1972 event in the Aghara paper. It should have been developed by the Langley Research Center since it is referred as 72 LaRC. Its differential form is:

$$\frac{d\Phi}{dE} = 2.2 \times 10^7 e^{\left(-\left(\frac{E-100}{30}\right)\right)} \tag{3.3}$$

This is not the differential form of Weibull function should look like and it is also not the double power law of the Band function. Therefore, it should be some form of the EXP function. The 1989 and 1991 events are both modeled by a Weibull function. The first is referred as 89 Weibull and the second one as 91 Carr. Its nonlinear regression fit parameters are given in Table 3.1 (Aghara, 2015). The differential forms of these events are as follows:

$$\frac{d\Phi}{dE} = \Phi_0 k\alpha \cdot E^{\alpha-1} e^{(-kE^{\alpha})} \tag{3.4}$$

The source is modeled as a pencil beam originated from a point located a certain distance from the target along Z-axis (Aghara, 2015).

It is important to specifically define the source in a transport code in order to perform an accurate normalization. This means that, the source flux should be defined in either differential or integral form i.e. J or $J(>E)$. FLUKA requires the source to be defined in differential form because this form doesn't change with a choice of energy step which the user is allowed to vary. If a source depends on the energy step, the magnitude of the result may vary with the choice of the energy step size. Differential flux, however, is by definition normalized by energy and is thus independent of the energy step size.

Table 3.1 Spectral Weibull parameters for two SPE events

Event	Φ_0	k	α
October 1989 (89 Weibull)	7.323×10^{11}	2.115	0.2815
March 1991 (91 Carr)	1.47×10^{12}	0.972	0.4410

The detector in the FLUKA simulation is modeled as a disk oriented normal to the flux of the incident particles. Vacuum is assigned to the detector region. This region is "floating" inside the Void region made also of vacuum which in turn is surrounded by a blackhole region. The detector's radius is 15 cm and its thickness is 0.5 cm. The detector thickness doesn't actually matter since it is a border between two regions (void and detector) which is used to measure the fluence. In fact, a separate region to score fluence is redundant because the border between the void and the target can be used as a detector. The reason to add an additional region is to accelerate the fluka run. The target is made of materials other than vacuum and they are computationally expensive. Therefore, suppressing the target and leaving only a "simple" vacuum detector allowed a high quality result to be acquired within a short timeframe.

The FLUKA validation purpose to make sure the proton fluence generated by FLUKA is identical to the source fluence and matches the fluence reported in the paper. The criterion for good agreement is determined in the following way. Both fluence reported in paper and fluence generated by FLUKA are plotted.

After the above equations of differential fluence (Eq (3.2)-(3.4))where converted into vector form and a source file for each event was generated by C++ code, the FLUKA's user routine read it and a simulation of proton fluence was generated by FLUKA. This simulated proton fluence was measured by the USRBDX detector. It is important to understand that there are two values, which theoretically should be identical:

(1) Fluence reported in the Aghara paper.

(2) Fluence scored by fluka detector.

Together were plotted for four SPE sources to determine how well was the USRBDX measurement. This comparison is shown in Figure 3.4, which contains four proton fluence spectra as they appear in the Aghara paper. It also shows how well the FLUKA simulation matches the source equation and how well both (FLUKA and equation) match the spectra reported by Aghara's paper.

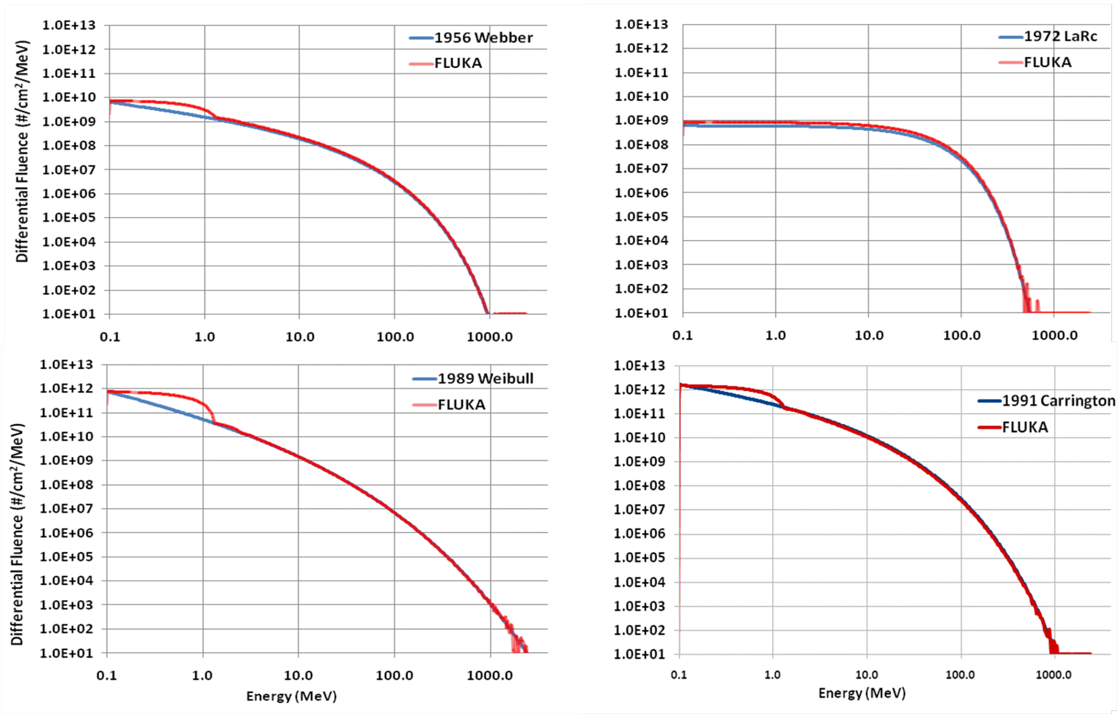

Figure 3.4 Fit of the FLUKA-generated fluences with fluences from the Aghara's paper.

In order to quantify the difference among these results a method of Mean Square Deviation (MSD) is utilized (Aghara, 2015):

$$MSD = \frac{1}{n}\sum_{i=0}^{n}(\theta_i - \theta_i')^2 \tag{3.5}$$

where θ and θ' are values from fluka and the Aghara's Paper; i is the energy spectral and n is the total number of values. The MSD values are summarized in Table 3.2 Note that the smaller numbers of MSD indicatea smaller difference (and better agreement) between two codes. Notice that for all four SPE cases the MSD values are small the results show that fluka source SPE agree better as compared to Fluences from the Aghara's Paper.

Table 3.2 MSD values for fluxes obtained by FLUKA, and from Aghara's paper

SPE event	FLUKA result vs Aghara's paper
56 Webber	0.024
72 LaRC	0.021
89 Weibull	0.028
91 Carrington	0.023

3.4 Normalization factor

For the source spectrum scoring, the output of the USRBDX card has units of part/cm^2/GeV/pr. The fluence in Figure 3.4, however is given in part/cm^2/MeV. The following is the conversion procedure:

$$\left[\frac{part}{(cm^2)(GeV)(pr)}\right]\left[\frac{1GeV}{10^3 MeV}\right]\left[A_d cm^2\right]\left[N\frac{pr}{cm^2}\right] \tag{3.6}$$

where A_d is the detector's area normal to flux and the fourth term is the normalization factor. Table 3.3 shows normalization parameters calculated for all four sources using eq.3.1. The detector's area is $\pi \cdot 15^2$ = 706.86 cm^2, were 15 is the detector's radius.

Table 3.3 Normalization factors for SPE source

SPE Event	Normalization factor (pr/cm^2)
56 Webber	9.5048e+09
72 LaRC	1.8439e+10
89 Weibull	4.0692e+11
91 Carr	1.0337e+12

The dose scoring from SPEs was achieved by employing the USRBIN scoring card. Unlike the USRBDX, which scores per area, the USRBIN card scores a 3-D region. The user is required to choose a grid (mesh) type that partitions the scoring region into elements or grid bins.There are several options for the grid's type. For a Cartesian grid, the user specifies the dimensions of a rectangular parallelepiped that encompasses a scoring region. Then, the user chooses the number of bins that fit along each dimension of that parallelepiped. Another type of the grid is cylindrical. In this case, the scoring region is a right circular cylinder.The default output of USRBIN is GeV/g/pr. To obtain the dose per primary particle, Gy/pr, the following conversion is necessary:

$$\left[\frac{GeV}{(g)(pr)}\right]\left[\frac{10^9 eV}{GeV}\right]\left[\frac{1.60218\times10^{-19}J}{1eV}\right]\left[\frac{10^3 g}{kg}\right]=\frac{Gy}{pr} \tag{3.7}$$

Next, a SPE normalization factor converts it into a dose as follows:

$$\left[\frac{Gy}{pr}\right]\left[N\frac{pr}{cm^2}\right]\left[A_d cm^2\right]\cdot 100 = cGy \tag{3.8}$$

where the second term is the same normalization factor as in Table 3.3. The third term is a cross-sectional area of the target perpendicular to flux.

The normalization factor in case of the raw GCR source can be calculated based on the two values provided by GCR package that can be found in the output file (.out), in the section called “Output during Transport.” These two values are Global Normalization (integral over energy and angle) called Fluxst and Equivalent Flux called Flux in the output file. The first value depends on the number of source ions chosen to be included into the source (number of .spc files involved) and has units of ions/cm^2/s. Notice the time unit appears in the normalization factor. The second value, the Flux, depends on the radius of the emission sphere and has units of part/pr/cm^2, where pr is primary mentioned earlier. The Flux value is basically the isotropic flux exposure to galactic cosmic radiation during a solar minimum divided by the surface area of the emission sphere. For the solar minimum, this flux equals to about 4 protons/cm^2/s (Jursa, 1985). A normalization factor is found by dividing Fluxst by Flux. The result is a quantity with units of pr/s. Therefore, multiplying this quantity by the USRBIN output (Gy/pr after some conversion), one should get the absorbed dose rate.

The fluence in figure 2.2 is given in ions/cm^2/s/sr/(MeV/amu), where amu is an atomic mass number of a given ion. The conversion from the USRBDX units (integral over solid angle) is as follows:

$$\left[\frac{part}{(cm^2)(GeV)(pr)}\right]\left[\frac{GeV}{10^3 MeV}\right]\left[\frac{1}{1/amu}\right]\left[\frac{10^4 cm^2}{m^2}\right]\left[\frac{1}{2\pi sr}\right]\left[\frac{pr}{s}\right]$$
$$= \frac{ions}{(m^2)(s)(sr)\frac{MeV}{amu}} \tag{3.9}$$

where sr stands for steradians. The last term is the normalization factor found, as explained earlier, by dividing the Fluxst by the Flux value found in the *.out file.
For GCRs dose scoring, the USRBIN card was set a bit differently. Instead of using mesh that divides the target into a number of bins, the scoring was done per region meaning a dose absorbed by a target as a whole was scored producing a single value as a result. Since the scoring is done per region, the output unit of the USRBIN card differ from the one used in SPEs USRBIN.The bins of the Cartesian and cylindrical grid have simple shapes and their volume is calculated analytically. When the scoring is done per region, the bins can be of any shape because regions can be described in any unpredictable ways. Consequently, unlike the case when the scoring is done with Cartesian or cylindrical grid, the output of the scoring per region is not normalized to the region volume. The output units of the USRBIN card in this case is the same unit as before but multiplied by region's volume [8]. The unit conversion to the dose rate is as follows:

$$\left[\frac{(GeV)(cm^3)}{(g)(pr)}\right]\left[\frac{1}{cm^3}\right]\left[\frac{10^9 eV}{GeV}\right]\left[\frac{1.60218\times 10^{-19} J}{1eV}\right]\left[\frac{10^3 g}{kg}\right]\left[\frac{pr}{s}\right][10^6\cdot 3600\cdot 24]$$
$$= \frac{\mu Gy}{day} \tag{3.10}$$

where the second term is divided by the region's volume, the 6th term is Fluxst/Flux and the last term is conversion to μGy and days.

CHAPTER 4

MODELING OF COSMICS RADIATION SHIELDING

Once FLUKA's source is validated, it is possible to start testing materials for their shielding properties. The first step is to set up a configuration that includes a target, a shield around it and a source (SPE and GCR).

4.1 Geometry for FLUKA

The traditional approach of transport codes to implement a geometry based on a Constructive Solid Geometry (CSG) which involves the boolean geometry tree - a hierarchical structure of the geometry elements. The basic idea is that any geometrical objects, regardless of their complexity, are made of elementary shapes (primitives) that can be added to or subtracted from one another to produce complex objects (Theis). Figure 4.1 demonstrates how CSG works. A combination of objects are joined into a region. A material is then applied to a region, not to an object. Each region can be made of only one material. Therefore, FLUKA's particles interact with regions, not objects itself. For example, it is mandatory to assign a special material called blackhole to a region where all particles vanish once they reach this region. Blackhole serves as a particle terminator because it has an infinite absorption cross section. For all fluka experiments performed for this paper, such a region was a sphere, which encompassed all other regions.

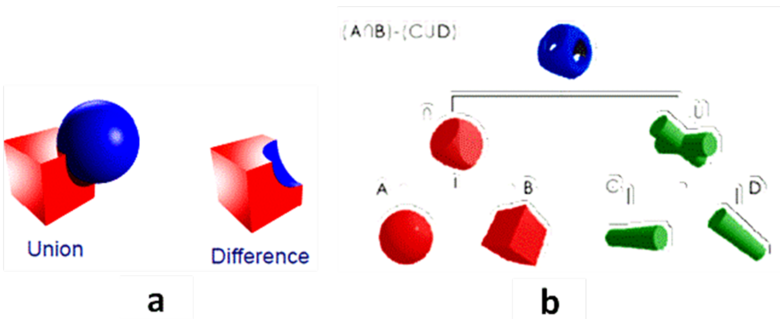

Figure 4.1 (a) Constructive Solid Geometry (b) example of a boolean geometry tree.

4.2 SPEs shielding

An important quantity in the absorption of radiation called areal density is a common way to measure thickness of a shield. The definition of areal density is mass per unit area of a two-dimensional object. Areal density is basically the shield's thickness times the density of the material of which shield is made:

$$A.D. = \rho \cdot t \tag{4.1}$$

Areal density is an intermediate step in conversion between thickness and mass of material behind given area and since dose is energy absorbed by a given mass, area density is more convenient than thickness. The target is a cylindrical body that consist of two parts: The materials shielding followed by a water slab (fig 4.2). The Shield has a thickness of 10 g/cm^2. This is a typical average wall thickness of the International Space Station and the Space Shuttle (Aghara, 2015). The water is 30 g/cm^2, which corresponds to the thickness of an average human body. In fact, there is a negligible difference in stopping power between water and tissue therefore water is commonly used as tissue equivalent.

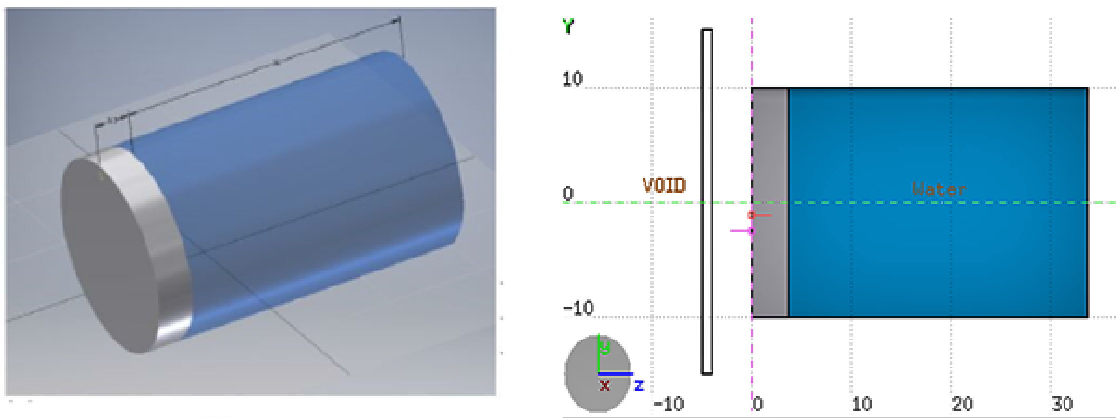

(a) (b)

Figure 4.2 Target for SPEs soure radiation shilding. (a) 3D model, (b) how it is modeled in FLUKA

The materials used for the simulation to determine the effectiveness of radiation shielding are hydrogen-rich and has low density materials with small atomic mass numbers because they are usually the most efficient shields for space radiation. Therefore

Liquid hydrogen, Water and Polyethylene was chosen to simulate and compare their effectiveness with aluminum – the primary metal used in spacecraft.

It is important to notice here that both geometrical thickness and mass of each layer varies with material but since the purpose of this experiment is to compare performance of different materials, some variable must stay constant. Here, such variable is area density. For linear geometry such as cylinder, fixed area density means that layers of different materials have different thicknesses while their masses are equal no matter what material they are made of. This is because a mass relates to the flux area linearly, which in turn is constant in case of cylinder. Each materials have the same area density 10 g/cm^2 and covers an area with radian 10 cm. The different density and thickness of all materials in this study are provided in Table 4.1.

Table 4.1 Density and thickness of each material in this simulation.

Material	Density(g/cm^3)	Thickness (cm)
Aluminum	2.7	3.7
Polyethylene	0.94	10.7
Water	1	10
Liquid hydrogen	0.07	143

Once the material was defined, a solar event for all farther experiments should be chosen.The obvious choice of a source SPE for material testing would be the largest one. In this study we chose four SPEs in 1956, 1972, 1989 and 1991 to simulate the efficiency of materials shielding. The distance of the emission source is 50 cm form the target and 5×10^7 events were simulated and repeated for15 runs.The figure 4.3 and 4.4 shows the amount of dose in the shield and target for the SPE1991 and SPE1972. The solid line shows the boundary between shield and target.The results of the FLUKA simulations were calculated the absorbed dose from SPE source proton beam. A water target of 30 cm long was used in order to simulate. The shield have 10 g/cm^2 for all materials.the hight dose is indicated by the dark color. Different doses in these figure are the result of spectra of primary source and shielding materials. The more discussion will be explain in the next chapter.

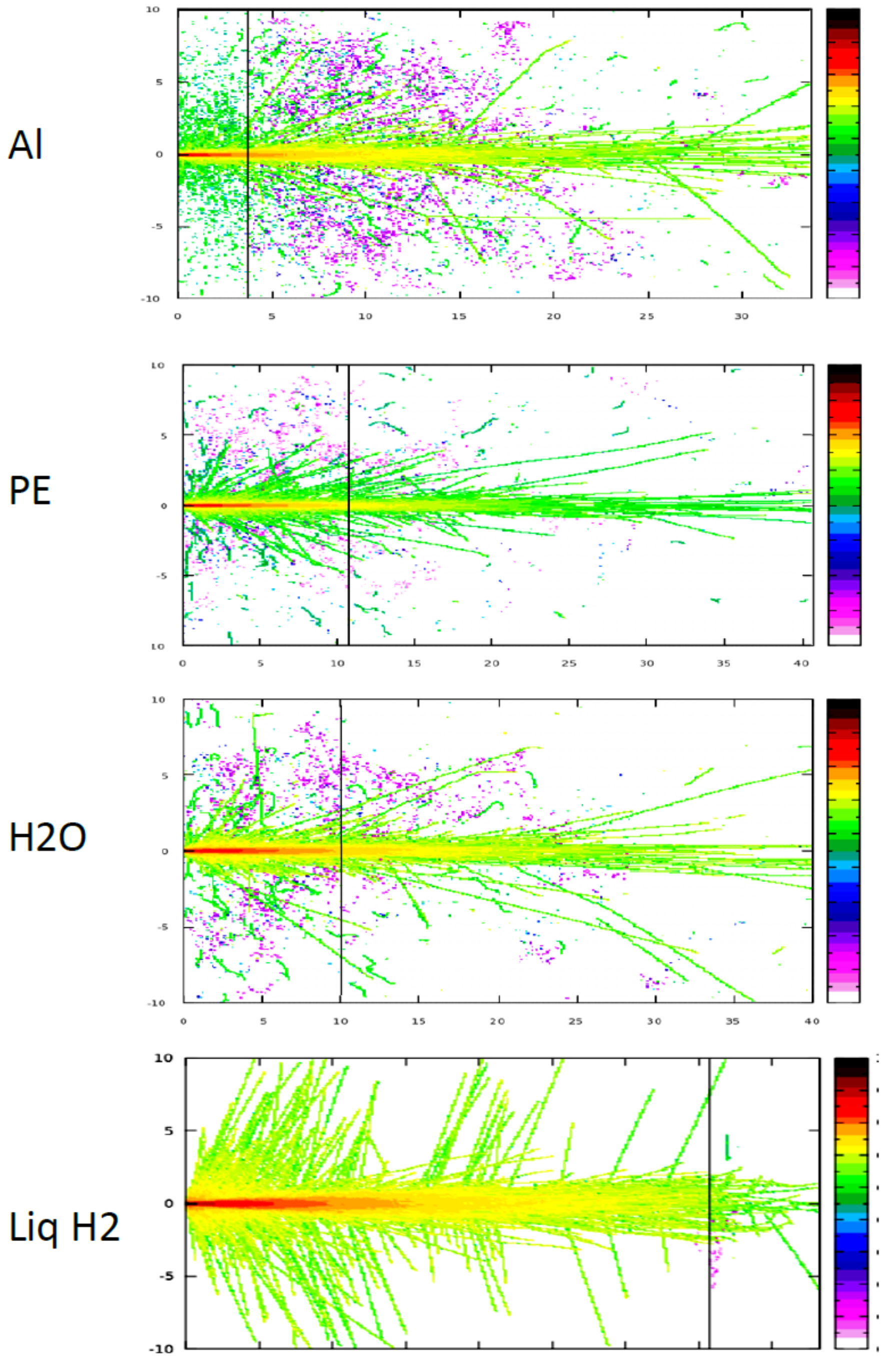

Figure 4.3 Absorbed dose values at various depths in water behind 10 g/cm^2 of different shielding materials for SPE 1991 environment.

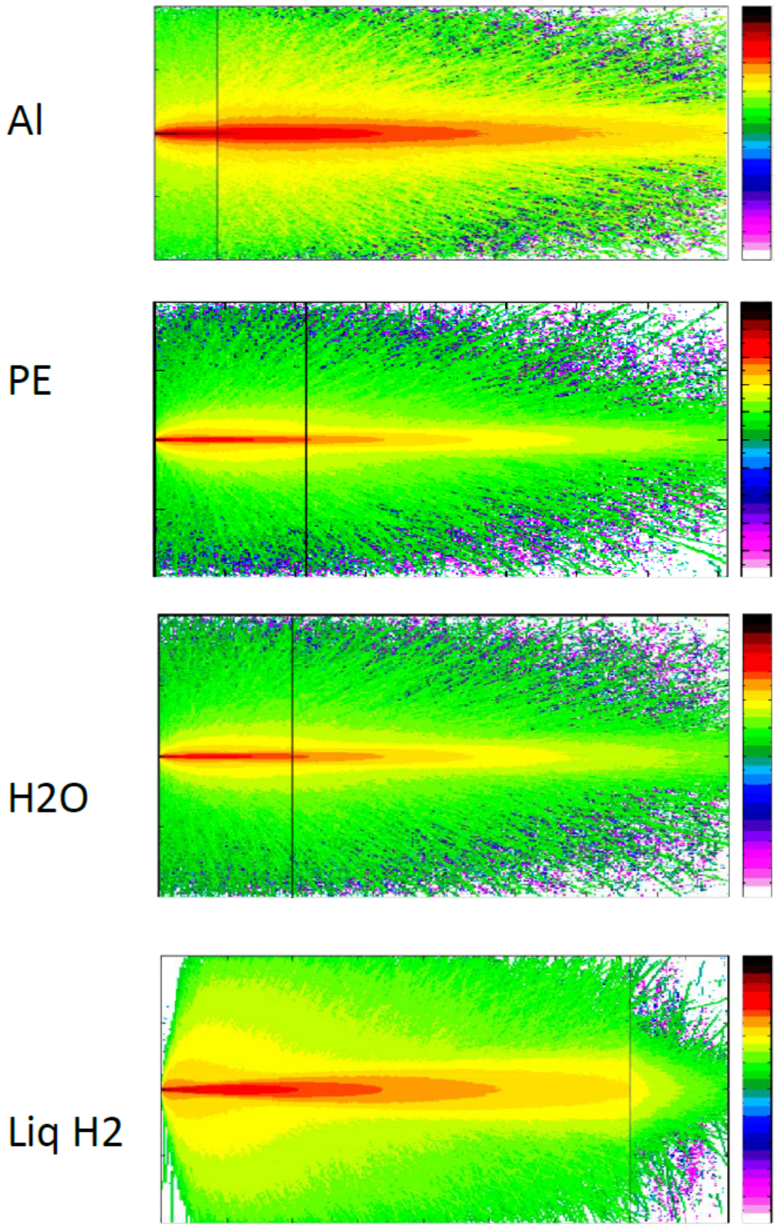

Figure 4.4 Absorbed dose values at various depths in water behind 10 g/cm^2 of different shielding materials for SPE 1972 environment.

4.3 GCRs shielding

This simulation was performed to determine effectiveness of different materials to shield from GCRs. The GCR source in Fluka is defined as an emission sphere instead of a pencil beam. Consequently, detectors and targets are also spheres instead of cylinders. The water target is a spherical with radius of 30 cm. inside a spherical shield. A single material was assigned to the shield with thickness of 10 g/cm ^{2} . The radius of the emission sphere is 80 cm. Four materials that the same as using in SPEs shielding were tested. The simplified model depicted in Figure 4.5. The dose absorbed by each layer was scored to get a dose distribution within the shield and water target. The source is uniform and isotropic fluence that consist of 28 ions: Z=1 to Z=28. Figure 3.3 shows the energy spectrum for the first four of these ions.

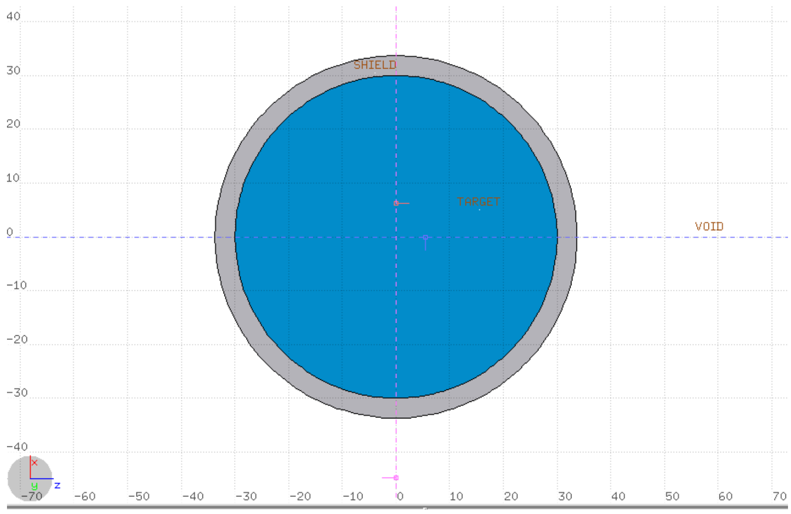

Figure 4.5 The Simplified Model to Obtain the Dose Profile Within the Shield from GCRs

CHAPTER 5
RESULTS AND CONCLUSION

5.1 Dose profiles due to SPEs

The first simulation is to study shielding characteristics of different materials for the SPE source. The target for this is a cylindrical body that consist of two parts: The materials shielding followed by a water slab (fig 4.2). The Shield has a thickness of 10 g/cm^2 (aluminum, polyethylene, water and liquid hydrogen) and the water thickness is 30 g/cm^2. The source are the large SPE four events in 1956, 1972, 1989 and 1991. Figure 5.1 shows absorbed dose at various depths inside different materials for four SPE events.

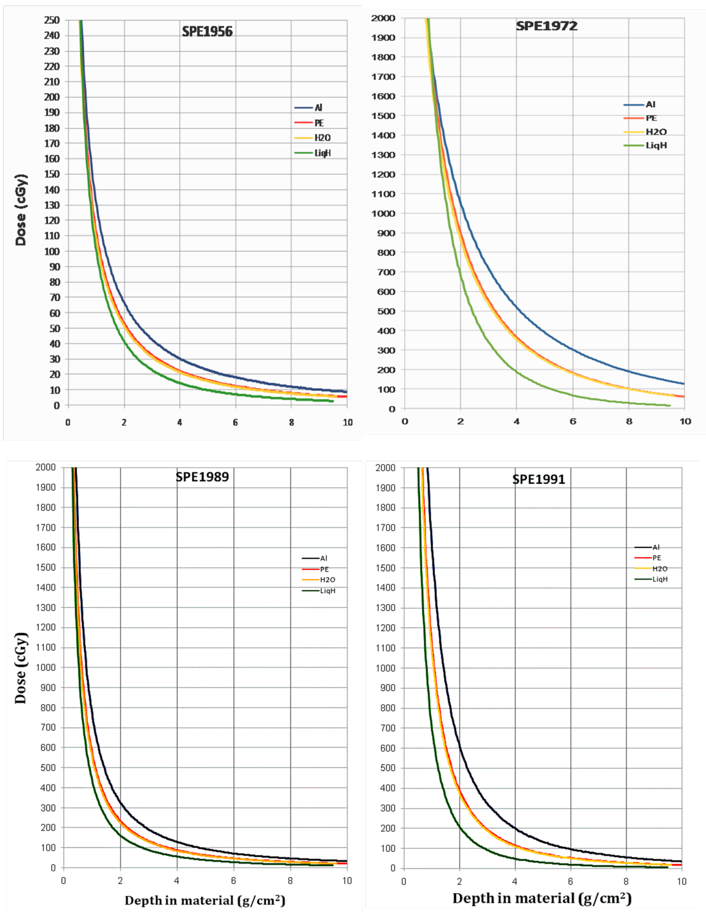

Figure 5.1 Dose profiles inside all material shielding of 10 g/cm^2 thickness

We see that all adsorbed dose decrease dramatically by increasing the shielding depths However, it can be seen that dose decreases very slowly when approaching 10 g/cm^2 for all materials.

To assess the effectiveness of shielding we will consider the dose as occurring in the water target. The figure 5.2 shows absorbed dose at various depths in water behind 10 g/cm^2 of each materials shield for all SPE environments. According to the results, it was found that the absorbed dose behind liquid hydrogen shield is smaller than dose in polyethylene, water and aluminum respectively. it can be concluded that for all solar event, the material's dose profiles are in accordance with the Z/Aρ of the material. The low density materials with small atomic mass numbers should be the most efficient material. Liquid hydrogen should be the most efficient material.

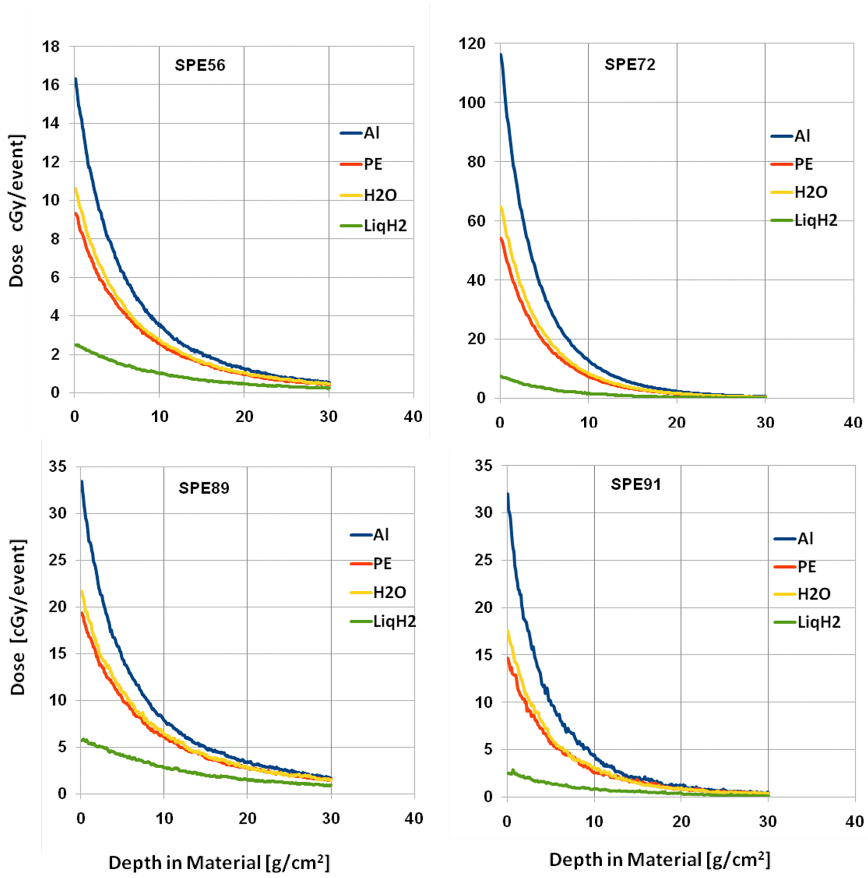

Figure 5.2 Dose distribution within the water slab shielded by 10 g/cm^2 of aluminum (Al), polyethylene (PE), water (H2O) and liquid hydrogen (Liq H2) for SPE 1956, 1972, 1983 and 1991.

The dose occurs in each SPEs differently as a result of different material make different secondary particles to generate dose. As for the target, it was important not only to get the total absorbed dose but also to understand what secondary particles, produced in the shield, contribute most to the total dose. Fluka allows to score dose specifically due to certain particle. If one knows what secondaries are produced in the shield, it is possible to determine how much each of these particles contribute to the total dose absorbed by the target. The run summary, found in the Fluka's output file, provide information about the secondary particles (Polkovnikov). It includes percentage breakdown for the secondaries abundance. The output file shows the following four energetic particles to be most abundant for all tested materials: protons, neutrons, photon and alpha particle. Therefore, the target dose is reported in terms of the dose components due to each of these particles.

Since SPE source was modeled only as a fluence of protons, any contribution to the target dose other than from protons must be due to secondary particles such as alpha, photon and neutrons. Figure 5.3 shows the fluence of the main target's dose contributors.

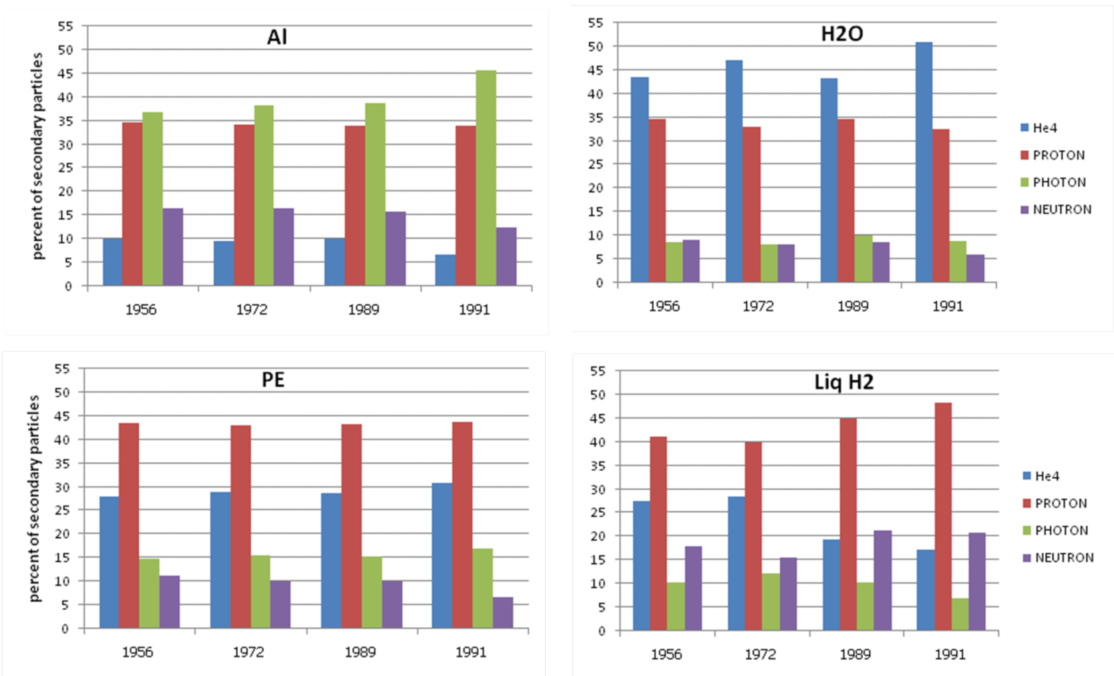

Figure 5.3 Percent of secondary particles in shield and target due to SPEs

To evaluate the effectiveness of radiation shielding materials. We use “The percent of dose reduction”in comparison.Table 5.1. shows the absorbed dose in unshielded and shielded target and the percent of dose reduction shows in table 5.2.and figure 5.4.

The results of our simulation in SPE sources show that the liquid hydrogen performances as radiation shielding material are as good as the Polyethylene, Water and Aluminum. Specifically, for the 10 g/cm^2 thicknesses we report average percent of dose reductions 99.0% for Liquid hydrogen 96.8% for Polyethylenethe 96.5 % for Water and 94.9% for Aluminum, respectively. These results are in agreement with the Z/Aρ of the material. The low density materials with small atomic mass numbers should be the most efficient material for radiation shielding.

Table 5.1 The absorbed dose in unshielded and shielded target

SPEs	No shielding	Al	H2O	PE	Liq H2
1956	27 cGy	2.34 cGy	1.72 cGy	1.58 cGy	0.58 cGy
1972	292 cGy	21.44 cGy	13.16 cGy	11.41 cGy	2.00 cGy
1989	314 cGy	10.14 cGy	7.70 cGy	7.22 cGy	3.16 cGy
1991	625 cGy	6.51 cGy	4.11 cGy	3.86 cGy	0.99 cGy

Table 5.2 Percent of dose reductions for SPEs shielding. Results are calculated from the difference between dose in unshielded and shielded target shown in table 5.1.

SPEs	Al	H2O	PE	Liq H2
1956	91.38%	93.66%	94.19%	97.88 %
1972	92.65%	95.49%	96.09 %	99.31%
1989	96.77 %	97.55 %	97.70%	98.99%
1991	98.96 %	99.34%	99.38%	99.84%

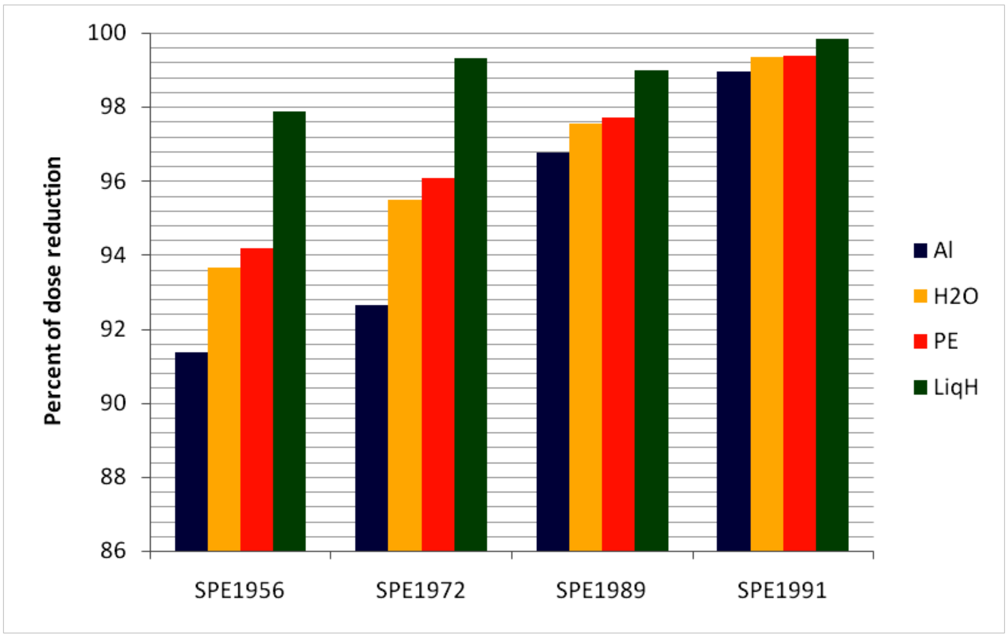

Figure 5.4 Percent of dose reductions for SPEs shielding.

5.2 Dose profiles due to GCRs

This simulation was performed to determine the effectiveness of different materials to shield from GCR in solar minimum and solar maximum. The source is uniform and isotropic fluence that consist of 28 ions from Z=1 to 28. Figure 3.3 shows the energy spectrum for the first four of these ions. Using the same shielding materials as before and the simplified model (figure4.5) with shield thickness of 10 g/cm^2. The target's absorbed doses are shown in figure 5.5. The results show that the absorbed dose in water target behind liquid hydrogen have the lowest value to the other test materials. These results are in agreement within SPE cases. The absorbed dose due to solar maximum are lower than solar minimum due to the flux of GCRs are modulated by solar energetic particles.

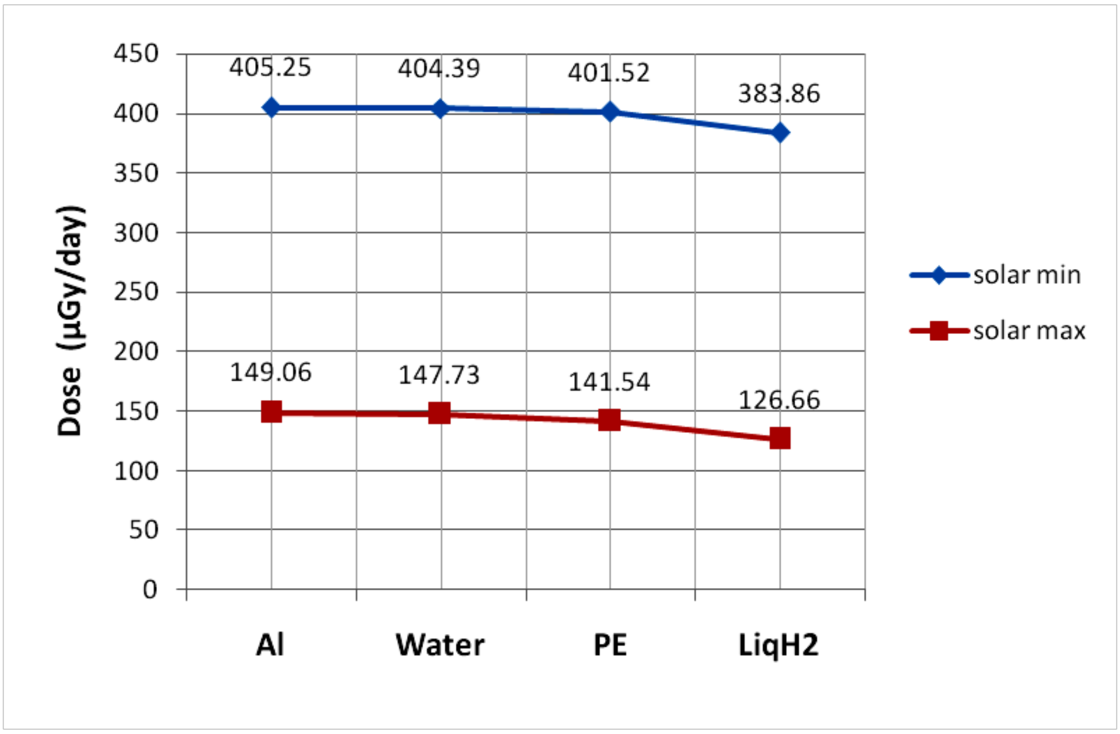

Figure 5.5 Dose absorbed by water target behind each materials shield due to GCRs in solar minimum and maximum

The first thing to notice here is the small difference absorbed dose for all tested materials. This is due to higher energies of GCR ions. Another thing to notice is that although protons are still dominant contributors to the target's dose. Also, other particles such as neutron, pions and α-particls show noticeable contribution compared to SPEs case. This means that GCRs creates a larger population of secondaries inside the shield and this adds more dose to the target. Figure5.6 shows percent of secondary particles inside shield and target due to GCRs for solar minimum and solar maximum.

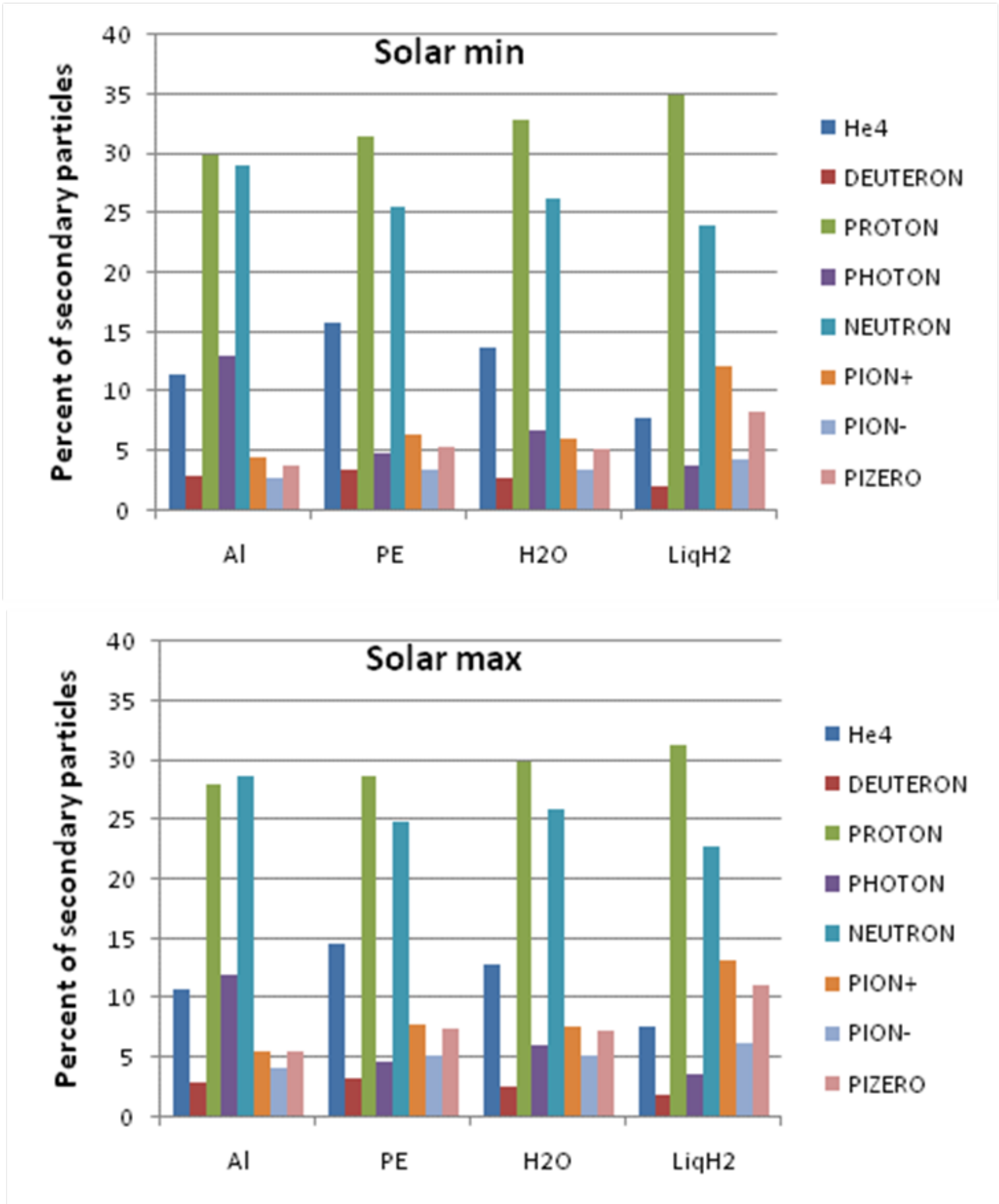

Figure 5.6 Percent of secondary particles inside shield and target due to GCRs for solar minimum and solar maximum.

5.3 Conclusion

The purpose of this study is to find materials that are advantageous in terms of radiation shielding in space. This radiation is one of the major obstacles to having a human presence in deep space. To evaluate the material's shielding property, the expected radiation environment was modeled. In this paper, one source of such radiation, Solar particles event (SPE) was simulated using the EXP, Weibull and Band model because this model has good agreement with observational data and allows us to model almost any SPE event happened in past sixty years.

There are different ways to evaluate the efficiency of different materials to attenuate radiation in space. Today several transport codes can simulate the necessary conditions and estimate the dose absorbed by target shielded by material of interest. This study employs the Monte Carlo code called FLUKA because of its high accuracy and availability. The advantage of FLUKA is that it models complex objects using the Constructive Solid Geometry Module and it has built-in tools to model the isotropic GCR environment. The GCR at solar minimum and solar maximum was chosen to simulate .

Before FLUKA was used for this study, its output was validated with the results reported in published papers. An intention of this study was to find a material that would outperform aluminum, the most prevalent material in spacecraft. The test model was chosen to be as realistic as possible but at the same time would not requiring too much computational time.

The results of our simulation in SPE and GCR sources show that liquid hydrogen, polyethylene and water,These are hydrogen-rich and has low density materials with small atomic mass numbers, better performance than aluminum at 10 g/cm^2 thickness.

The GCR source was modeled as a fluence of 28 ions. It was found that the choice of material used for shielding from GCR has much smaller effect on the efficiency of a shield than the case of SPE source due to higher energies of GCR ions.

REFERENCES

REFERENCES

ACES. **Advanced Cosmic Explorer database.** Pasadena: California Institute of Technology, 2015.

Adams, J. and et al. **Revolutionary Concepts of Radiation Shielding for Human Exploration of Space.** Alabama: NASA Marshall Space Flight Center, 2005.

Aghara, S.K. and et al. "Shielding evaluation for solar particle events using MCNPX, PHITS and OLTARIS codes", **Life Sciences in Space Research.** 2(4): 79-91; January, 2015.

Alankrita, M. **Galactic Cosmic Ray Exposure of Humans in Space Influence of galactic cosmic ray models and shielding on dose calculations for low-Earth orbit and near-Earth interplanetary space.** Doctor's Thesis: Kiel University, 2013.

Atwell, W. and et al. "Spectral Analyses and Radiation Exposures from Several Ground-Level Enhancement (GLE) Solar Proton Events: A Comparison of Methodologies", in **41st International Conference on Environmental Systems.** p.3240. Portland: Curran Associates Inc., 2011.

Badavi, F. and et al. "Evaluation of the new radiation belt AE9/AP9/SPM model for a cis lunar mission", **Acta Astronautica.** 40(102): 156–168; October, 2014.

"modeling human exposure to space radiation with different shielding: The fluka code coupled with anthropomorphic phantoms", **Journal of Physics: Conference Series.** 3(41): 135-142; June, 2006.

Belov, A. and et al. "Coronal Mass Ejections and Non-recurrent Forbush Decreases", **Solar Physics.** 289(10): 3949-3960, April, 2014.

Bohr, N. "LX. on the decrease of velocity of swiftly moving electrified particles in passing through matter", **Philosophical Magazine Series 6.** 30(178): 581-612; December, 1915.

"On the Constitution of Atoms and Molecules", **Philosophical Magazine Series 6.** 26(151): 1-25; July, 1913.

REFERENCES (CONTINUE)

Christian, E.R., Cummings, A.C. and Stone, E.C. "Evidence for Anomalous Cosmic Ray Hydrogen", **The Astrophysical Journal**. 334(2): L77-L80; August, 1988.

Cucinotta, F. and et al. **Radiation Risk Acceptability And Limitations.** Washington DC: NASA Technical Information Service, 2010.

Evaluating Shielding Approaches to Reduce Space Radiation Cancer Risks. Washington DC: NASA Technical Information Service, 2012.

Space radiation cancer risk projections and uncertainties. Washington DC: NASA Technical Information Service, 2013.

Dietze, and et al. "Assessment of radiation exposure of astronauts in space", **Annals of the ICRP.** 42(4): 1–339; August, 2013.

Dova, M.T. "Ultra-High Energy Cosmic Rays", in **CERN–Latin-American School of High-Energy Physics.** Peru: CERN, 2013.

Ferrari, A. and et al. **FLUKA: a multi-particle transport code (Program version 2008).** Geneva: CERN, 2005.

Fisk, L.A., Kozlovsky, B. and Ramaty, R. "An Interpretation of the Observed Oxygen and Nitrogen Enhancements in Low-Energy Cosmic Rays", **Astrophysical Journal**. 190: L35-L37; May, 1974.

Garcia-Munoz, M., Mason, G.M. and Simpson, J.A. "A New Test for Solar Modulation Theory: the 1972 May-July Low-energy Galactic Cosmic-ray Proton and Helium Spectra", **Astrophysical Journal.** 182: L81-L84; June, 1973.

Greisen, K. "End to the Cosmic-Ray Spectrum?", **Physical Review Letters.** 16(17): 748-750; April, 1966.

Hovestadt, D. and et al. "Differential Energy Spectra of Low-Energy (<8.5 MeV/Nuc) Heavy Cosmic Rays During Solar Quiet Times", **Physical Review Letters.** 31(10): 650-654; September, 1973.

Hüfner, J. "Heavy fragments produced in proton-nucleus and nucleus-nucleus collisions at relativistic energies", **Physics Reports.** 125(4): 129–185; August, 1985.

REFERENCES (CONTINUE)

NCRP. **Information needed to make radiation protection recommendations for space missions beyond low-earth orbit.** Bethesda MD: National Council on Radiation Protection and Measurements, 2006.

Jokipii, J.R. "Particle Acceleration at a Termination Shock. I - Application to the Solar Wind and the Anomalous Component", **Journal of Geophysical Research**. 91(A3): 2929-2932; March, 1986.

Jursa, A. "GALACTIC COSMIC RADIATION AND SOLAR ENERGETIC PARTICLE", **Handbook of geophysics and the space environment.** United States Air Force, 1985.

Kim M. (2012) "Scientist of the Month", http://www.dsls.usra.edu. March 20, 2018.

Kim M. and et al. "Issues for simulation of galactic cosmic ray exposures for radiobiological research at ground-based accelerators", **Front Oncol.** 5(122): 1-14; June, 2015.

Klecker, B. "The Anomalous Component of Low-Energy Cosmic Rays: a Comparisonof Observed Spectra with Model Calculations", **Journal of Geophysical Research**. 82(32): 5287-5291; November, 1977.

Kobetich, E., Katz, J. and Jun, R. "Energy deposition by electron beams and σ-rays", **Physical Review Journal.** 170(2): 391–396; June, 1968.

Leo, W. R. **Techniques for Nuclear and Particle Physics Experiments.** Berlin: Springer Verlag, 1994.

Lowenstein, D. and Rusek, A. "Technical developments at the NASA Space Radiation Laboratory", **Radiat Environ Biophys.** 46(2): 91-94; June, 2007.

Marsden, R.G. and et al. **Anomalous Cosmic Ray.** Belgium: Kluwer Academic Publishers, 1998

McDonald, F.B.and et al. "The Anomalous Abundance of Cosmic Ray Nitrogen and Oxygen Nuclei at Low Energies", **Astrophysical Journal.** 187: L105-L108; February, 1974.

Mewaldt, R. "Galactic cosmic ray composition and energy spectra", **Advances in Space Research.** 14(10): 737-747; October, 1994.

REFERENCES (CONTINUE)

Mrigakshi, A. and et al. “How galactic cosmic ray models affect the estimation of radiation exposure in space”, **Advances in Space Research.** 51(5): 825–834; March, 2013.

NASA. **Human exploration research opportunities: Ground based studies in space radiobiology.** Washington DC: NASA Technical Information Service, 2015.

NASA. **NASA space flight human system standard. Volume 1: Crew health.** Washington DC: NASA Technical Information Service, 2007.

National Research Council. **Pathways to exploration-rationales and approaches for a U.S. Program of Human Space Exploration.** Washington DC: National Academies Press, 2014.

NCRP. “Operational Radiation Safety Program for Astronauts in Low-Earth Orbit: a Basic Framework”, **NCRP report.** 142, 2002.

Norbury, J. and Slaba, T. “Space radiation accelerator experiments-The role of neutrons and light ions”, **Life Sciences in Space Research.** 3: 90–94; October, 2014.

Olive, K.L. and et al. “Review of particle physics”, **Chinese Physics C.** 40(10): 378-379; October, 2016.

Pesses, M.E., Jokipii, J.R. and Eichler, D. “Cosmic Ray Drift, Shock Wave Acceleration and the Anomalous Component of Cosmic Rays”, **Astrophysical Journal**. 246: L85-L88; January, 1981.

Porta, A. and Agosteo, S. “Double-differential spectra of secondary particles”, **Radiation Protection Dosimetry.** 132(1): 29–41; December, 2008.

Townsend, L. W. “Implications of the Space Radiation Environment for Human Exploration in Deep Space”, **Radiation Protection Dosimetry.** 115(1-4): 44-50; December, 2005.

Townsend, L.W. “Radiation Protection Guidance for Activities in Low-Earth orbit”, **Advances in Space Research.** 30(4): 957-963; November, 2002.

REFERENCES (CONTINUE)

Mountford, P.J. and Temperton, D.H. “Recommendations of the International Commission on Radiological Protection (ICRP) 1990”, **European Journal of Nuclear Medicine.** 19(2): 77–79; February, 1992.

Reames, D.V., Barbier, L.M. and Von Rosenvinge, T.T. “WIND/EPACT Observations of Anomalous Cosmic Rays”, **Advances in Space Research.** 19(5): 809-812; July, 1997.

Rojdev, K. and Atwell, W. **Hydrogen-and Methane-Loaded Shielding Materials for Mitigation.** Pasadena: American Society for Gravitational and Space Research, 2014.

Sauer, H.H., Zwicki, R.D. and Ness, M.J. **Summary Data for the Solar Energetic Particle Events of August through December 1989.** Tokyo: Space Environment Laboratory, 1990.

Schiavi, A. **Study of Laser Produced Plasmas by X-Ray and Proton Radiography.** London: University of London, 2003.

Shea, M.A. and Smart, D.F. “A Summary of Major Solar Proton Events”, **Solar Physics.** 127(2): 297-320; June, 1990.

Slaba, T. and et al. **GCR simulator reference field and a spectral approach for laboratory simulation.** Washington DC: National Aeronautics and Space Administration, 2015.

Stone, E.C. and Cummings, A.C. “Evidence for Anomalous Cosmic Ray S, Si, and Fe in the Outer Heliosphere and for a Non-ACR Source of S at 1 AU”, in **25th Intern Cosmic Ray Conference.** p.289. Durban: Potchefstroom University, 1997.

Swordy, S. “The energy spectra and anisotropies of cosmic rays”, **Space Science Reviews.** 99(1-4): 85-94; October, 2001.

Takashima, T. and et al. “The First Observation of Sulfur in Anomalous Cosmic Rays by the GEOTAIL and the WIND Spacecraft”, **Astrophysical Journal**. 477(2): L111-L113; March, 1997.

Theis, C. “Basic steps with SimpleGeo”, **SimpleGeo.** http://flukacourse.web.cern.ch. March 1, 2018.

REFERENCES (CONTINUE)

Turner, J. E. **Atoms, Radiation, and Radiation Protection,** 3rd ed. Weinheim: Wiley, 2007.

Tylka, A., Dietrich, W. and Atwell, W. "Assessing the Space-Radiation Hazard in Ground-Level Enhanced (GLE) Solar Particle Events", in **2010 Fall AGU Meeting.** San Francisco: Moscone Convention Center, 2010.

Von Rosenvinge, T.T., and McDonald, F.B. "IMP 6, 7, and 8 Observations of the Composition and Time Variations of Low Energy Cosmic Rays", in **14th International Cosmic Ray Conference.** p.792. Munich: Max-Planck Institut for Extraterrestrische Physik, 1975.

Wilson, W. J. and et al. **Workshop on Shielding Strategies for Human Space Exploration.** Hampton: Langley Research Center, 1997.

Xapsos, M. and et al. "Characterizing Solar Proton Energy Spectra for Radiation Effects Applications", **IEEE Transactions on Nuclear Science.** 47(6): 2218-2223; December, 2000.

Zatsepin, G.T. and Kuz'min, V.A. "Upper Limit of the Spectrum of Cosmic Rays", **Journal of Theoretical Physics Letters.** 4(3): 78-80; August, 1966.

Zeitlin, C. "Physical interactions of charged particles for radiotherapy and space applications", **Health Physics.** 103(5): 540-546; November, 2012.

Zeitlin, C. and et al. "Measurements of energetic particle radiation in transit to Mars on the Mars science laboratory", **Science.** 340(6): 1080-1084; May, 2013.

APPENDIX

MONTE CARLO METHOD

When one hears the name Monte Carlo, one often thinks of the gambling locale in the country of Monaco. It is the home of the famous Le Grand Casino as well as many other gambling resorts and Formula One Racing. This chapter, however, is not about gambling or racing. It is, however, about a concept that underlies gambling, that is, probability, hence, its association and designation with the well-known gambling region. The scientific study of probability concerns itself with the occurrence of random events and the characterization of those random happenings. Gambling casinos rely on probability to ensure, over the long run, that they are profitable. For this to happen, the odds or chance of the casino winning has to be in its favor. This is where probability comes into play because the theory of probability provides a mathematical way to set the rules for each one of its games to make sure the odds are in its favor . As a simulation technique, Monte Carlo simulation relies very heavily on probability.

Monte Carlo simulation, also known as the Monte Carlo method, originated in the 1940s at Los Alamos National Laboratory. Physicists Stanislaw Ulman, Enrico Fermi, John von Neumann, and Nicholas Metropolis had to perform repeated simulations of their atomic physics models to understand how these models would behave given the large number of uncertain input variable values. As random samples of the input variables were chosen for each simulation run, a statistical description of the model output emerged that provided evidence as to how the real-world system would behave. It is this concept of repeated random samples of model input variables over many simulation runs that defines Monte Carlo simulation . Essentially, we are creating an artificial world (model) that is meant to closely resemble the real world in all relevant aspects.

Monte Carlo simulation is often superior to a deterministic simulation of a system when that system has input variables that are random. Deterministic simulations are referred to as what-if simulations. In these simulations, a single value is chosen for each input random variable (a particular what-if scenario) based on a best guess by the modeler. The simulation is then run and the output is observed. This output is a single value or a single set of values based on the chosen input. But because the input variables are random variables, they can take on any number of values defined by their probability distributions. So to have a sense of how the system would respond over the complete range of input values, more than one set of inputs must be evaluated. Monte Carlo simulation randomly samples values from each input variable distribution and uses that sample to calculate the model's output. This process is repeated many times until the modeler obtains a sense of how the output varies given the random input values. One should readily see that when the simulation contains input random variables, Monte Carlo simulation will yield a result that is likely to be more representative of the true behavior of the system. The next section formally defines Monte Carlo simulation and provides examples of its use.

When setting up a Monte Carlo simulation or employing the Monte Carlo Method, one follows a four step process. These four steps are:

Step 1) Define a distribution of possible inputs for each input random variable.

Step 2) Generate inputs randomly from those distributions.

Step 3) Perform a deterministic computation using that set of inputs.

Step 4) Aggregate the results of the individual computations into the final result.

While these steps may seem overly simplistic, they are necessary to capture the essence of how Monte Carlo simulations are set up and run. This four-step method requires having the necessary components in place to achieve the final result. These components may include:

(1) probability distribution functions (pdfs) for each random variable

(2) a random number generator

(3) a sampling rule, a prescription for sampling from the pdfs

(4) scoring, a method for combining the results of each run into the final result

(5) error estimation, an estimate of the statistical error of the simulation output as a function of the number of simulation runs and other parameters.

Step 1) requires the modeler to match a statistical distribution to each input random variable. If this distribution is known or sufficient data exist to derive it, then this step is straightforward. However, if the behavior of an input variable is not well understood, then the modeler might have to estimate this distribution based on empirical observation or subject matter expertise.

The modeler may also use a uniform distribution if he or she is lacking any specific knowledge of the variable's characteristics. When additional information is gathered to define the variable, then the uniform distribution can be replaced.

Step 2) requires randomly sampling each input variable ' s distribution many times to develop a vector of inputs for each variable. Suppose we have two input random variables X and Z . After sampling n times, we have X = $(x_1, x_2, \ldots, x_n)$ and Z = $(z_1, z_2, \ldots, z_n)$. Elements from these vectors are then sequentially

chosen as inputs to the function defining the model. The question of how large n should be is an important one because the number of samples determines the power of the output test statistic. As the number of samples increases, the standard deviation of the test statistic decreases. In other words, there is less variance in the output with larger sample sizes. However, the increase in power is not linear with the number of samples. The incremental improvement of power decreases by a factor of about $1/\sqrt{n}$, so there is a point when more sampling provides little improvement. Determining the number of trials needed for a desired accuracy is addressed below.

Step 3) is straightforward. It involves sequentially choosing elements from the randomly generated input vectors and computing the value of the output variable or variables until all n outputs are generated for each output variable.

Step 4) involves aggregating all these outputs. Suppose we have one output variable Y . Then we would have as a result of step 4 an output vector Y = $(y_1, y_2, \ldots, y_n)$. We can then perform a variety of statistical tests on Y to analyze this output.

The following is a simple example of how this method works.

Example : Determining the Value of Pi

Recall that the value of Pi (π) is the ratio of a circle' s circumference to its diameter. To calculate this value, we can set up a Monte Carlo simulation that employs a geometric representation of the circle.

(1) To start, draw a unit circle arc, that is, an arc of radius one circumscribed by a square as shown in Figure A.1.

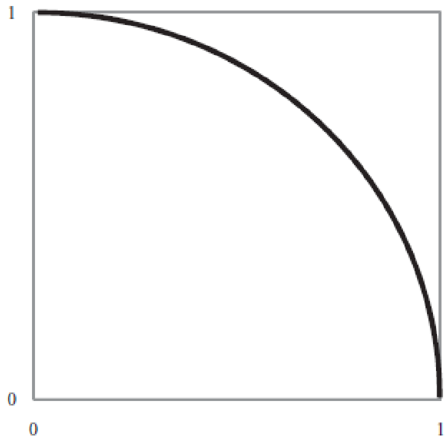

Figure A.1 Unit circle arc for calculation of π

(2) Then, randomly choose an x and y coordinate inside the square, and place a dot at that location.

(3) Repeat step 2 at a given number of times. See Figure A.2.

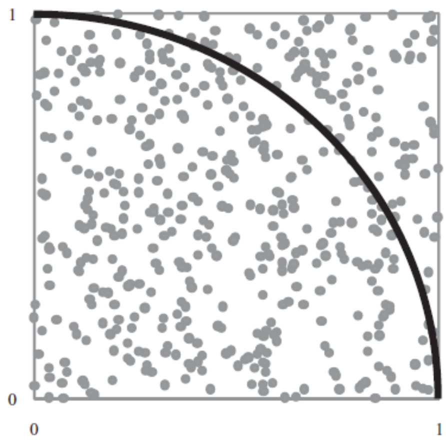

Figure A.2 Random dots placed inside the square.

(4) Count the total number of dots inside the square and the number of dots inside the quarter circle. With a large number of dots generated, these values will approximate the area of the circle and the area of the square. From mathematics, this result can be represented as ability density function.

$$\frac{\#\text{ of dots inside circle}}{\#\text{ of dots inside square}} = \frac{\frac{1}{4}\pi r^2}{r^2} = \frac{1}{4}\pi \tag{A.1}$$

A sampling rule existed that used the random numbers to select values from the uniform distribution. The scoring method was given by the formula in step 4 above. Finally, error estimation can be performed by comparing the computed value of π to an authoritative source for its value. This simulation can be set up using a spreadsheet and the built in functions of rand() that generates uniform random numbers between 0 and 1 and the countrify (range, criteria) function that can count the number of random numbers that meet the specify ed criteria. The author generated 500 uniform random numbers between zero and one for the x coordinate of each point and the same for the y coordinate. These numbers were paired up and plotted. Precisely 340 of the 500 points fell inside the circle giving a simulated value for π of 2.76. This method produced an error of 12.1 percent. Using a larger set of generated dots can help reduce the error to an acceptable range realizing that it requires a trade - off for extra computation.

From this example, you can see the necessary components that are central to Monte Carlo simulations. These components are one or more input random variables, one or more output variables, and a function that computes the outputs from the inputs. This configuration is shown in Figure A.3.

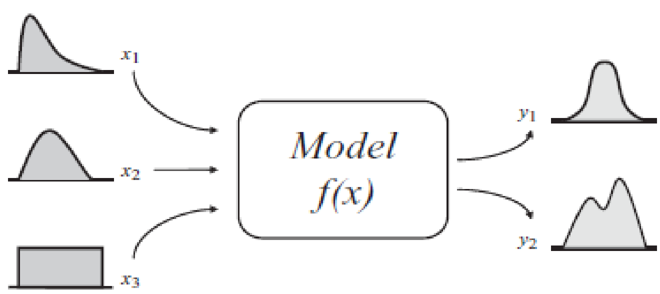

Figure A.3 Basic Monte Carlo model.

In this figure, notice that there are three input random variables x_1, x_2 and x_3 , all with different distributions. There are two output variables, y_1 and y_2 , that have resulting distributions created by the repeated sampling of the input and feeding those samples into the function $f(x)$.

VITAE

NAME	MR. DUMRONGSAK RODPHOTHONG
EDUCATION	YEAR 2003-2007 KASETSART UNIVERSITY
	BACHELOR OF SCIENCE (PHYSICS)
	YEAR 2009-2012 UBON RATCHATHANI UNIVERSITY
	MASTER OF SCIENCE (PHYSICS)
E-MAIL	dumrongsak.ro.55@ubu.ac.th